May 2017

Novel Nanomaterials for Lithium Ion Batteries and Oxygen Reduction Reactions

Jianyang Li
University of Wisconsin-Milwaukee

NOVEL NANOMATERIALS FOR LITHIUM ION BATTERIES AND OXYGEN REDUCTION REACTIONS

by

Jianyang Li

A Dissertation Submitted in

Partial Fulfillment of the

Requirements for the Degree of

Doctor of Philosophy

in Engineering

at

The University of Wisconsin-Milwaukee

May 2017

ABSTRACT

NOVEL NANOMATERIALS FOR LITHIUM ION BATTERIES AND OXYGEN REDUCTION REACTIONS

by

Jianyang Li

The University of Wisconsin-Milwaukee. 2017
Under the Supervision of Professor Chris Yuan

Undoubtedly, one of the most pressing issues that world is dealing with today is global warming. It requires long-term potential actions for sustainable development to achieve solutions to address this kind of environmental problems that we are facing today. In this regard, renewable energy resources appear to be the one of the most efficient and effective solutions to reduce reliance on fossil fuels that cause release of excess amounts of carbon dioxide, the main contributor to global warming. As an alternative, electrochemical energy production has long been explored due to its intrinsic nature of more sustainable and more environmentally friendly. Lithium-ion batteries and fuel cells are two of the most studied systems for electrochemical energy storage and conversion. Although the energy storage and conversion mechanisms of lithium-ion batteries and fuel cells are different, there are “electrochemical similarities” of these two systems, all consisting of two electrodes in contact with an electrolyte solution. In order to improve the electrochemical performance of rechargeable lithium-ion batteries, various anode materials including Si and Sn have attracted tremendous interests to replace currently used graphite anode due to their high theoretical specific capacity. However, up to 400% volume

expansion/contraction causes cracking and pulverization leading to repaid capacity fading during charge and discharge process. On the other side, the searching of advanced nanocatalysts with unprecedented catalytic efficiency at low-cost limps toward commercialization of highly efficient fuel cells and lithium-air batteries, whereas the pivotal challenges lie in the kinetically sluggish oxygen reduction reaction (ORR) at the cathode.

Nanostructured materials have offered new opportunities to design high capacity lithium-ion battery anodes and efficient catalysts to replace traditional noble metal such as Pt based materials. The objective of this study is to demonstrate high performance anode with superior rate capacity and long-cycle-life and effective nanocatalyst for oxygen reduction reaction with superior electrocatalytic activity and stability through rational design of novel nanomaterials. First, a three-dimensionally interconnected carbon nanotube/layered MoS_2 nanohybrid network is reported with best-so-far rate capability and outstanding long cycle life. The monolayer and bilayer MoS_2 ultrathin nanosheets with large surface to volume ratio facilitate fast Li ion transport further boosting high power capability, while incorporating high conductive CNT enhances the electronic conductivity and retains the structural integrity. The nanohybrid delivers discharge capacity as high as 512 mAh g^{-1} at 100 A g^{-1} and 1679 mAh g^{-1} over 425 cycles at 1 A g^{-1} with 96% discharge capacity retention of the initial cycle.

Then a novel 3D carbon coated Si NPs loaded on high conductive ultrathin graphene nanosheets was fabricated for potential use as anode material for high performance LIBs. The unique structural design of Si@C/NRGO has the combined merits of the carbon layer coating and graphene nanosheets which not only provides volume buffer and improve the conductivity but also separates the Si particles from direct exposure to electrolyte to form a stable SEI layer. Thus, the Si@C/NRGO nanohybrid demonstrates a superior electrochemical performance which

is an ideal candidate for high performance LIBs. The nanohybrid delivers discharge/charge capacity of 3079 and 2522 mAh g^{-1} in the initial cycle at 100 mA g^{-1}, corresponding to a Coulombic efficiency of 82%. A reversible capacity of 2312 mAh g^{-1} with an approximate Coulombic efficiency of 92% is retained when the current density increases to 1 A g^{-1} at the 3rd cycle. After 250 cycles, the nanohybrid still retains charge capacity of 1525 mAh g^{-1}, close to a 60% capacity retention of the first cycle at 100 mA g^{-1}. Moreover, the Si@C/NRGO nanohybrid demonstrates proficient cyclic stability with reversible capacities of 1932, 1507, and 1245 mAh g^{-1} for 2, 4, and 8 A g^{-1}, respectively.

Subsequently, a three-dimensionally core-shell structured edge enriched Fe_3C@C nanocrystals on graphene network is demonstrated with superior electrocatalytic activity and stability. The graphene nanosheets provide host and vital support for locally grown edge enriched Fe_3C nanocrystals, which in-turn perform like separator/spacer to avoid the stacking of ultrathin graphene sheets, leading to a high surface area and super-stable Fe_3C@C/rGO hybrid structure. The unique structural design of Fe_3C@C/rGO nanohybrid with large surface area enables fast mass transport and a large number of active sites for catalytic reactions. The Fe_3C@C/rGO nanohybrid exhibits excellent ORR catalytic activity with a high positive onset potential close to 1.0 V, a Tafel slope of 65 mV/decade, and excellent durability with only ~8% current density decay at 0.8 V after 20,000 seconds' continuous operation, which is superior to that of a commercial Pt/C in an alkaline electrolyte.

To

my parents,

my wife,

and especially my daughter and my son

TABLE OF CONTENTS

LIST OF FIGURES

ACKNOWLEDGMENTS

First and foremost, I would like to express my deepest appreciation and thanks to my PhD advisor, Professor Dr. Chris Yuan, for his overwhelming support in the past five plus years. He has always been supportive for me both academically and financially. But more importantly he gave me the freedom to pursue various projects without objection. So, I have the opportunity to explore and work on multiple projects during my PhD years including but not limited to the memorable experience in the UWM industrial assessment center (IAC) and Johnson Controls – UWM Energy Advancement Research Lab, which let me to build a strong connection with the scientists from JCI. I would also like to thank my committee members, Professor Dr. Junhong Chen, Professor Dr. Benjamin Church, Professor Dr. Deyang Qu and Professor Dr. Arsenio Pacheco for serving as my committee members even at hardship. It was always a pleasure to discuss the projects or classes with them. The way they teach and guide their students influenced me a lot. Thank them all for their suggestions to improve my thesis and research. I wish them all the best in their future life.

I would also like to thank all my co-workers, colleagues in the LSNM lab, and all my friends at UWM and in this beautiful city. My life became a lot easier with their help and encouragement.

A special thanks to my family. There are no words that can express how grateful I am to my wife for all the sacrifices that she has made on my behalf. She's always on my side, and ready to help in any way she can so I can focus on my study and research. I would also like to thank my two beautiful kids, Grace and David, for all the tears and smiles they bring to me. The

financial support from my father-in-law and mother-in-law helped me out in the past few years, especially the tremendous efforts and time my mother-in-law spent to take care my two kids.

CHAPTER 1 INTRODUCTION AND RESEARCH OBJECTIVES

1.1 Introduction

It is widely accepted that global warming is caused by the accumulation of greenhouse gases in the atmosphere arising from the combustion of fossil fuels and that they must be substantially reduced in order to prevent climate change.[5] Achieving solutions to environmental problems that we face today requires long-term potential actions for sustainable development. In this regard, renewable energy resources appear to be the one of the most efficient and effective solutions to reduce reliance on fossil fuels that cause release of excess amounts of carbon dioxide, the main contributor to global warming. The limitations of traditional clean energy sources including solar and wind are either undulating or intermittent because of variable weather conditions, which thus essentially requires large-scale energy storage devices to counterbalance its variability.[6] [5]As an alternative, electrochemical energy production has long been explored due to its intrinsic nature of more sustainable and more environmentally friendly. Lithium-ion batteries and fuel cells are two of the most studied systems for electrochemical energy storage and conversion. Although the energy storage and conversion mechanisms of lithium-ion batteries and fuel cells are different, there are “electrochemical similarities” of these two systems, all consisting of two electrodes in contact with an electrolyte solution. [7]

1.2 Nanostructured anodes for high performance lithium ion batteries

Rechargeable lithium ion batteries (LIBs) have long been explored as promising power sources for a wide variety of applications especially on portable electronics, electric vehicles, and stationary energy storage.[8, 9] In the search of high energy density anode materials, Si and Sn as promising candidates have attracted tremendous interests to replace currently used graphite anode due to their high theoretical specific capacity. However, up to 400% volume expansion/contraction causes cracking and pulverization leading to repaid capacity fading during charge and discharge process.[8, 10-12] Graphene analogue molybdenum disulfide (MoS_2) stands out as an alternative because of its relatively high-lithium-storage capacity (~670 mAh g^{-1}) and significantly less volumetric expansion upon lithiation/delithiation.[13, 14] The weak interlayer bonding (van der Waals interaction) and large interlayer spacing allow for the easier diffusion of Li^+ ions without significant volume change.[15, 16] Despite the intermediate lithiation voltage, the key drawback of employing MoS_2 as LIB electrode is its poor electronic conductivity.[17] Various approaches have been attempted to address this issue to improve cycling performance including stacking with graphene or its derivatives,[18-22] and coating on carbon nanotubes (CNTs) or other conductive materials,[23-31] and even mixing with multiwall CNTs (MWCNTs).[32] Among these, CNTs as ideal supporting material has been widely investigated for the fabrication of MoS_2 based composites due to its excellent electric conductivity, good mechanical property, high surface area, and low cost. Direct growth of MoS_2 on the surface of CNTs provides a promising perspective and demonstrates limited improvements in electrochemical performance partially due to the relatively low MoS_2 concentration.[24, 29, 31] Another possible reason is that semiconducting MoS_2 sheaths block the direct contact between conductive CNTs, which is unfavorable for fast electron transport,

thus leading to continuous capacity fading even at low current densities.[24, 31] Therefore, constructing a composite material with high content of MoS_2 and interconnected electron pathway are crucial for high rate capability and long term cyclability.

1.3 Efficient Nanocatalysts for Oxygen Reduction Reactions

The searching of advanced nanocatalysts with unprecedented catalytic efficiency at low-cost limps toward commercialization of highly efficient fuel cells and lithium-air batteries, whereas the pivotal challenges lie in the kinetically sluggish oxygen reduction reaction (ORR) at the cathode.[33-35] Although Pt-based materials have long been investigated for ORR due to their superior electrocatalytic activity,[35-37] the large-scale application has been hampered due to their high cost, low abundance, low stability, and also the issue of methanol crossover.[38-40] Inspired by the pioneering work on cobalt phthalocyanine (CoPe),[41] numerous efforts have been made to explore alternative catalysts based on non-precious metals (Fe, Co, etc.) [42-44] and metal-free materials [45, 46]. Among them, Fe–N/C complex electrocatalysts have attracted considerable attention as noble-metal-free electrocatalysts for the ORR owing to their low cost and high catalytic activity.[47-49] Despite extensive efforts and rapid progress, it remains a great challenge but desirable to develop porous Fe–carbon nanocatalysts with high surface area for fast mass transport and substantially exposed edge sites for effective catalytic reactions.

1.4 Thermodynamics and Kinetics of Oxygen Electrocatalysis

A direct four-electron pathway in aqueous alkaline media:

$$O_2 + 2H_2O + 4e^- \rightleftarrows 4OH^-$$

$$E^0 = 0.401 \text{ V vs SHE}$$

where E^0 is the standard reduction potential of O_2 to OH^-, versus Standard Hydrogen

Electrode (SHE).

Alternatively, a two-electron pathway where peroxide ion as intermediate agent,

$$O_2 + H_2O + 2e^- \rightleftarrows HO_2^- + OH^-$$

$$E^0 = -0.076 \text{ V vs SHE}$$

Followed by either further reduction

$$HO_2^- + H_2O + 2e^- \rightleftarrows 3OH^-$$

$$E^0 = 0.878 \text{ V vs SHE}$$

or disproportionation

$$2HO_2^- \rightleftarrows 2OH^- + O_2$$

The Nernst equation is used to calculate the equilibrium potential of oxygen electrode reactions in nonstandard conditions:

$$E = E^0 - \frac{RT}{nF} \ln \frac{a_{Ox}}{a_{Red_2}}$$

where R is the gas constant, T is the temperature, n is the number of electrons transferred, F is the Faraday constant, and a is activity of the oxidized and reduced species. Specifically, the electrode potential in alkaline media at 25 °C and at an O_2 pressure of 1 atm from Ag/AgCl to the reversible hydrogen electrode (RHE) potential:

$$E_{RHE} = E_{Ag/AgCl} + 0.059\ pH + E^o_{Ag/AgCl}$$

where E_{RHE} is the converted potential versus RHE, $E_{Ag/AgCl}$ is the measured experimental potential versus the Ag/AgCl reference electrode, and $E^o_{Ag/AgCl}$ is the standard potential of Ag/AgCl at 25 °C (0.1976 V).

To evaluate the ORR activity, it is only effective to use those methods based on convective/forced transport of reactants due to the low solubility of O_2 ($1.26 \times 10{-}3$ mol $L{-}1$) in the aqueous solutions. Thus, the rotating-disk electrode (RDE) technique becomes a powerful

tool on evaluating the electroactivity of ORR catalysts. For the RDE measurement, working electrodes were prepared following the same method as CV's. The polarization curves for ORR were scanned cathodically with a rate of 5 mVs^{-1} at various rotating speed from 400 rpm to 2025 rpm. The number of electrons transferred (*n*) and kinetic currents (J_k) were calculated using the Koutecky−Levich equation:

$$\frac{1}{J} = \frac{1}{J_L} + \frac{1}{J_K} = \frac{1}{B\omega^{1/2}} + \frac{1}{J_K}$$

Where J is the experimental measured current density, J_K and J_L are the kinetic-limiting and diffusion-limiting current densities, ω is the angular velocity, and B is Levich slope giving by

$$B = 0.62nFC_0{D_0}^{2/3}\nu^{-1/6} \qquad J_K = nFkC_0$$

where n is transferred electron number, F is the Faraday constant (96,500 $C \cdot mol^{-1}$), C_0 is the bulk concentration of O_2 (1.2×10^{-6} mol cm^{-3}), D_0 is the diffusion coefficient of O2 in the electrolyte (1.9×10^{-5} cm s^{-1}), *v* is the kinematic viscosity of the electrolyte (0.01 cm^2 s^{-1}), and k is the electron-transfer rate constant.

1.5 Research Objectives of This Proposal

The overall objective of the proposed research is to demonstrate novel nanomaterials for high performance lithium-ion batteries and oxygen reduction reactions through structural design. In order to achieve this research objective, there are few major tasks summarized below.

Task 1. Synthesis and characterization of three-dimensionally interconnected carbon nanotube/layered MoS_2 nanohybrid network with superior rate capacity and long-cycle-life.

The objective of this task is to synthesis three-dimensionally interconnected carbon nanotube/layered MoS_2 nanohybrid network with superior rate capacity and long-cycle-life for lithium-ion batteries. Several subtasks have been explored:

Surface functionalization of CNTs under argon and ammonia gas.

Continuous treatment of CNTs in concentrated HNO_3 (70% W/W) at 60 °C to further improve the hydrophilicity.

Synthesis of MoS_2/CNT nanohybrid using hydrothermal method.

Material characterization using various techniques, such as field emission scanning electron microscope (FESEM), transmission electron microscope (TEM), powder X-ray diffraction (XRD), Raman spectrometer, multipoint BET N_2 adsorption/desorption method (Micromeitrics ASAP200), thermal gravity analysis (TGA, TA SDT 2960), X-ray photoelectron spectroscopy (XPS), Fourier transform infrared (FT-IR) spectrophotometer, and Zeta Potential Analyzer.

The electrochemical performance of as prepared samples was characterized by CR2032-type coin cells.

Cyclic voltammetry (CV) and AC impedance were measured on a VersaSTAT 3F (Princeton Applied Research) electrochemical station.

Task 2. Synthesis and characterization of 3D carbon coated Si NPs loaded on high conductive ultrathin graphene nanosheets for potential use as anode material for high performance LIBs.

A novel 3D carbon coated Si NPs loaded on high conductive ultrathin graphene nanosheets is fabricated for potential use as anode material for high performance LIBs. The unique structural design of Si@C/NRGO has the combined merits of the carbon layer coating and graphene nanosheets which not only provides volume buffer and improve the conductivity but also separates the Si particles from direct exposure to electrolyte to form a stable SEI layer. Thus, the

Si@C/NRGO nanohybrid demonstrates a superior electrochemical performance which is an ideal candidate for high performance LIBs. Several subtasks have been explored:

Synthesis of Si@C/NRGO using commercial Si NPs, in-house graphene oxide, and low cost egg white solution.

Prepare the egg white derived carbon coating on Si NPs for controlled experiment.

Material characterization using various techniques, such as field emission scanning electron microscope (FESEM), transmission electron microscope (TEM), powder X-ray diffraction (XRD), Raman spectrometer, multipoint BET N_2 adsorption/desorption method (Micromeitrics ASAP200), thermal gravity analysis (TGA, TA SDT 2960), X-ray photoelectron spectroscopy (XPS), Fourier transform infrared (FT-IR) spectrophotometer, and Zeta Potential Analyzer.

The electrochemical performance of as prepared samples was characterized by CR2032-type coin cells.

Cyclic voltammetry (CV) and AC impedance were measured on a VersaSTAT 3F (Princeton Applied Research) electrochemical station.

Task 3. Synthesis and and characterization of three-dimensionally core-shell structured edge enriched Fe_3C@C nanocrystals on graphene network for oxygen reduction reaction with superior electrocatalytic activity and stability

The graphene oxide (GO) was synthesized through chemical exfoliation of graphite powders using a modified Hummers' method.

Prepare $Fe(NO_3)_3$@rGO powders.

Synthesis of Fe_3C@C/rGO.

Synthesis of Fe_3C@C.

Material characterization using various techniques, such as field emission scanning electron microscope (FESEM), transmission electron microscope (TEM), powder X-ray diffraction (XRD), Raman spectrometer, multipoint BET N_2 adsorption/desorption method (Micromeitrics ASAP200), thermal gravity analysis (TGA, TA SDT 2960), X-ray photoelectron spectroscopy (XPS), and Zeta Potential Analyzer.

A CH Instruments 600D electrochemical workstation operated in a standard three-electrode configuration was used to conduct the CV and LSV.

CHAPTER 2 A THREE-DIMENSIONALLY INTERCONNECTED CARBON NANOTUBE/LAYERED MoS_2 NANOHYBRID NETWORK WITH SUPERIOR RATE CAPACITY AND LONG-CYCLE-LIFE

2.1 Introduction

Rechargeable lithium ion batteries (LIBs) have long been explored as promising power sources for a wide variety of applications especially on portable electronics, electric vehicles, and stationary energy storage.[8, 9] In the search of high energy density anode materials, Si and Sn as promising candidates have attracted tremendous interests to replace currently used graphite anode due to their high theoretical specific capacity. However, up to 400% volume expansion/contraction causes cracking and pulverization leading to repaid capacity fading during charge and discharge process.[8, 10-12] Graphene analogue molybdenum disulfide (MoS_2) stands out as an alternative because of its relatively high-lithium-storage capacity (~670 mAh g^{-1}) and significantly less volumetric expansion upon lithiation/delithiation.[13, 14] The weak interlayer bonding (van der Waals interaction) and large interlayer spacing allow for the easier diffusion of Li^+ ions without significant volume change.[15, 16] Despite the intermediate lithiation voltage, the key drawback of employing MoS_2 as LIB electrode is its poor electronic conductivity.[17] Various approaches have been attempted to address this issue to improve cycling performance including stacking with graphene or its derivatives,[18-22] and coating on carbon nanotubes (CNTs) or other conductive materials,[23-31] and even mixing with multiwall CNTs (MWCNTs).[32] Among these, CNTs as ideal supporting material has been widely investigated for the fabrication of MoS_2 based composites due to its excellent electric conductivity, good mechanical property, high surface area, and low cost. Direct growth of MoS_2 on the surface of CNTs provides a promising perspective and demonstrates limited

improvements in electrochemical performance partially due to the relatively low MoS_2 concentration.[24, 29, 31] Another possible reason is that semiconducting MoS_2 sheaths block the direct contact between conductive CNTs, which is unfavorable for fast electron transport, thus leading to continuous capacity fading even at low current densities.[24, 31] Therefore, constructing a composite material with high content of MoS_2 and interconnected electron pathway are crucial for high rate capability and long term cyclability.

Herein, we present a novel and simple approach to the synthesis of three-dimensional (3D) messoporous nanohybrid network composed of one-dimensional (1D) CNTs and two-dimensional (2D) ultrathin layered MoS_2 nanosheets. Integrating of CNTs not only can improves the electronic conductivity of the nanohybrid, but also be able to reduce the MoS_2 nanosheets stacking to form well separated ultrathin film leading to significant increase of active surface area. The ultrathin MoS_2 nanosheets with large surface area shortens Li ions diffusion length which will benefit the rate capability.[14, 26] Moreover, interconnected high conductive CNTs act like backbones to constrain the volume change enabling structural integrity during charge/discharge process. Benefiting from aforementioned unique 3D structures, the MoS_2/CNT nanohybrid delivers superior electrochemical performance in terms of specific capacity, rate performance and long-term cycling stability. Such a unique all-solution-based approach thus provides a powerful avenue of rationally design of simple, low cost and scalable MoS_2/CNT anode materials with high rate capability toward practical industrial manufacturing.[50]

2.2 Experimental section

2.2.1 Surface Functionalization of CNTs

CNTs (Flo Tube 6000) with an average outer/inner diameter of 7 nm / 3 nm and length of 10 um were purchased from CNano Technology, Ltd. (San Francisco, CA) and functionalized

prior use. To start with, certain amount of CNTs was first annealed at 550 ^{o}C for 2 h under Argon and Ammonia gas (flow rate 100 sccm) in a conbustion boat. Afterwards, the sample was sonicated in concentrated HNO_3 (70% W/W) at 60 ^{o}C for 1hr to further improve the hydrophilicity.[51] After that the CNTs was washed with deionized (DI) water and dried at 60 ^{o}C in vaccum oven for overnight. 200 mg surface functionalized CNTs were dispersed in 1000 ml sodium dodecylbenzene sulfonate (SDBS) solution (0.2‰ w/w) with sonication for 1 hour and stored as carbon source for future use.

2.2.2 Synthesis of MoS_2/CNT nanohybrid

In a typical synthesis of the MoS_2/CNT nanohybrid, 151 mg sodium molybdate, 200 mg thiourea, and 25 ml CNT solution from step one were added in 45 ml DI water and sonicated for 30 minutes. The homogenous solution was then transferred to a Teflon-lined autoclave and heated at 250 °C for 24 h. The dark suspension (Figure S2b) was filtered and washed with DI water for several times before dried in vacuum oven.

For comparison, MoS_2 was synthesized by the similar hydrothermal method without adding carbon source. Other concentration composites (90%, 60%, 30%) were fabricated following the same way.

2.2.3 Material Characterization

The morphology and structure properties were observed using a Hitachi S-4800 field emission scanning electron microscope (FESEM) and a Hitachi H9000 NAR transmission electron microscope (TEM) operating at an acceleration voltage of 300 KV. The crystal structure and phase information were collected by powder X-ray diffraction (XRD) using Bruker D8 Discover A25 diffractometer with copper K_{α} radiation. Raman spectra were taken on a Renishaw 1000B Raman spectrometer with a 632.8 nm HeNe laser source. Surface area and CNT

concentration were measured by a multipoint BET N_2 adsorption/desorption method (Micromeitrics ASAP200) and thermal gravity analysis (TGA, TA SDT 2960), respectively. Further investigation on the compositions and atomic valence states was carried out on HP 5950A X-ray photoelectron spectroscopy (XPS) with Mg Kα as the source and the C 1s peak at 284.6 eV as an internal standard. Fourier transform infrared (FT-IR) spectra were collected with a Bruker Vector spectrophotometer with a resolution of 4 cm^{-1} with 40 scans per spectrum. Zeta potentials were measured in water (pH value ~7) by ZetaPals Zeta Potential Analyzer (BIC, NY).

2.2.4 Electrochemical Evaluation

The electrochemical performance of as prepared samples was characterized by CR2032-type coin cells, which were assembled in an argon-filled glove box with moisture and oxygen concentrations below 1.0 ppm. 1.0 M $LiPF_6$ in ethylene carbonate/ethyl methyl carbonate (40:60, v/v) was employed as electrolyte and lithium discs as the counter electrode and reference electrode. The electrodes were prepared following the standard industrial testing procedure. Slurry composed of 80 wt.% of active material, 10 wt.% of Super P conductive carbon black, and 10 wt.% carboxymethyl cellulose (CMC) was coated onto 18 um copper foil using automatic thick film coater (AFA-IV, MTI Co.). After the electrode completely dried, the foil was cut into 1/4 inch disks as working electrode. The low current density charge-discharge tests were performed on a LAND CT2001A (Land, China) battery tester and large rate characterizations were evaluated on Arbin BT-2000 system (USA) within the voltage range of 0.01 V and 3.0 V. Cyclic voltammetry (CV) and AC impedance were measured on a VersaSTAT 3F (Princeton Applied Research) electrochemical station.

2.3 Results and discussion

The synthetic procedure is schematically illustrated in Figure 1.1a, primarily based on simple hydrothermal method with the presence of surface functionalized CNTs. Detailed surface functionalization information can be found in experimental section (Supporting Information). The CNTs were fist annealed at 550 ^{o}C in argon and ammonia gas flow, followed by sonication in concentrated nitric acid and then dissolved in 0.1% (w/w) sodium dodecylbenzene sulfonate (SDBS) solution. Afterwards, sodium molybdate and thiourea were added in the homogenous solution of highly-dispersed surface functionalized CNTs (0.12 mg mL^{-1}). During the nanosheets formation process, the randomly-oriented CNTs provide vital support for the film growth a0nd simultaneously act as separator avoiding the ultrathin sheets stacking. Meanwhile, the cumulative generation of ammonia and heat treatment could continuously remove carboxyl, hydroxyl groups (generated by HNO_3 treatment, Figure S1.1) and surface reactants to yield purified high conductive CNTs.[51-53]

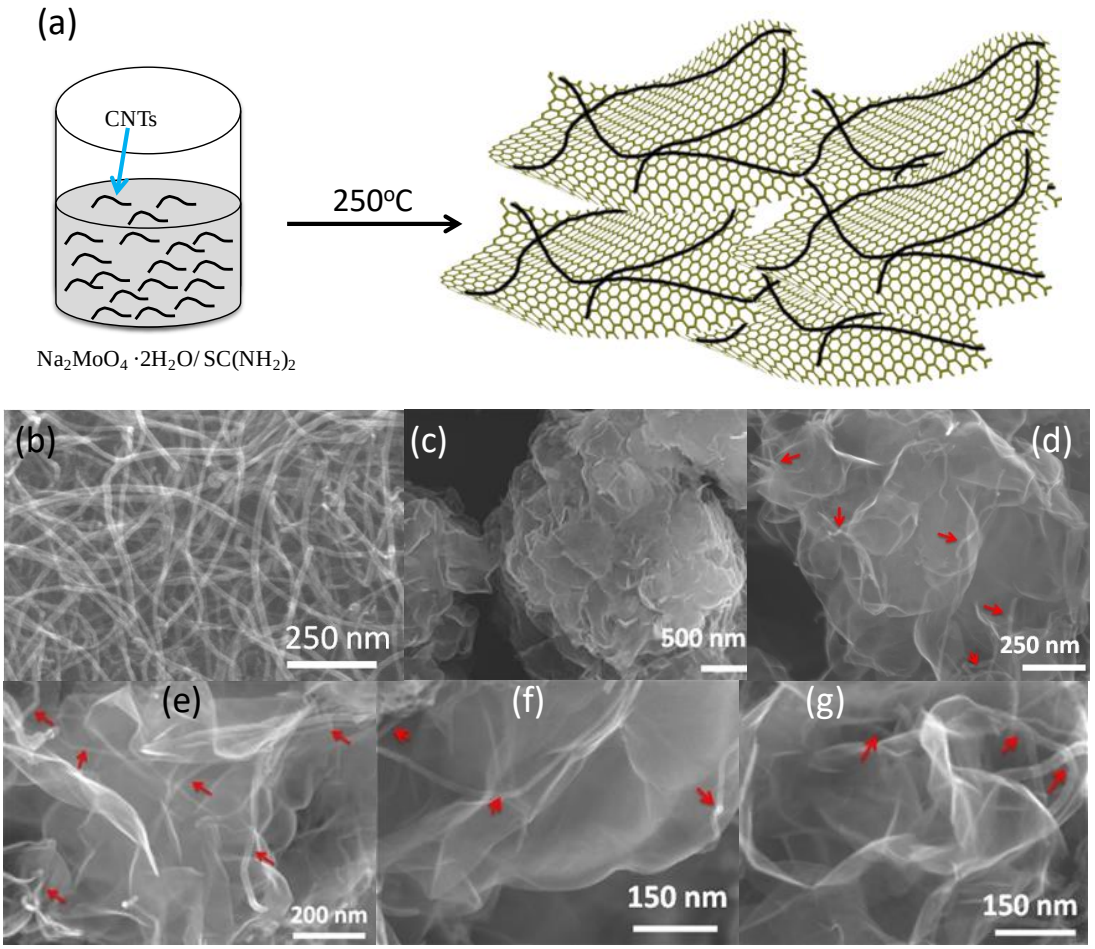

Figure 2.1 (a) Schematic illustration of synthesis process for MoS_2/CNT nanohybrid. FESEM images of (b) surface functionalized CNTs, (c) MoS_2, and (d-g) MoS_2/CNT nanohybrid. Arrows indicate CNTs in final product.

The field emission scanning electron microscopy (FESEM) study shows that without the presence of CNTs the MoS_2 sheets stack together to form dense flakes (Figure 2.1c, Figure S1.2a, S1.2d). Incorporation of CNTs with average outer diameter of 7 nm and length of 10 um (Figure 2.1b, Figure S1.2c) can effectively reduce the stacking and yield highly separated ultrathin MoS_2 nanosheets (Figure 2.1d-g, Figure S1.2b), which are later determined to be mostly of monolayer and bilayer. More importantly, the relatively long CNTs form interconnected network to

facilitate the fast electron transport during lithiation/delithiation process. It is clearly observed that different layers of crumpled MoS_2 nanosheets are supported/separated by randomly dispersed interconnected CNTs (marked by arrows). This unique architecture is anticipated to dramatically increase the electronic conductivity and maintain structural integrity thus to boost the rate performance and cycling stability in LIB applications.

The crystal structure and phase information of CNT, MoS_2 and MoS_2/CNT nanohybrid were investigated using X-ray diffraction (XRD) (Figure 2.2a). Both MoS_2 and MoS_2/CNT show the distinct diffraction peaks of a hexagonal crystal structure, which can be indexed as 2H-MoS_2 with space group of $P6_3/mmc$ (JCPDS 37-1492). Compared with pristine MoS_2, the (002) peak of nanohybrid displays a reduced intensity and broadened width, indicating the mean crystallite size of the MoS_2 in nanohybrid is much smaller than that of the pristine MoS_2. No other impurity was detected on both spectra. However, no noticeable diffraction peaks of CNT could be observed probably due to its low concentration. Thermogravimetric analysis (TGA) confirms that the amount of CNTs in the nanohybrid is about 7 wt% (Figure S1.3).

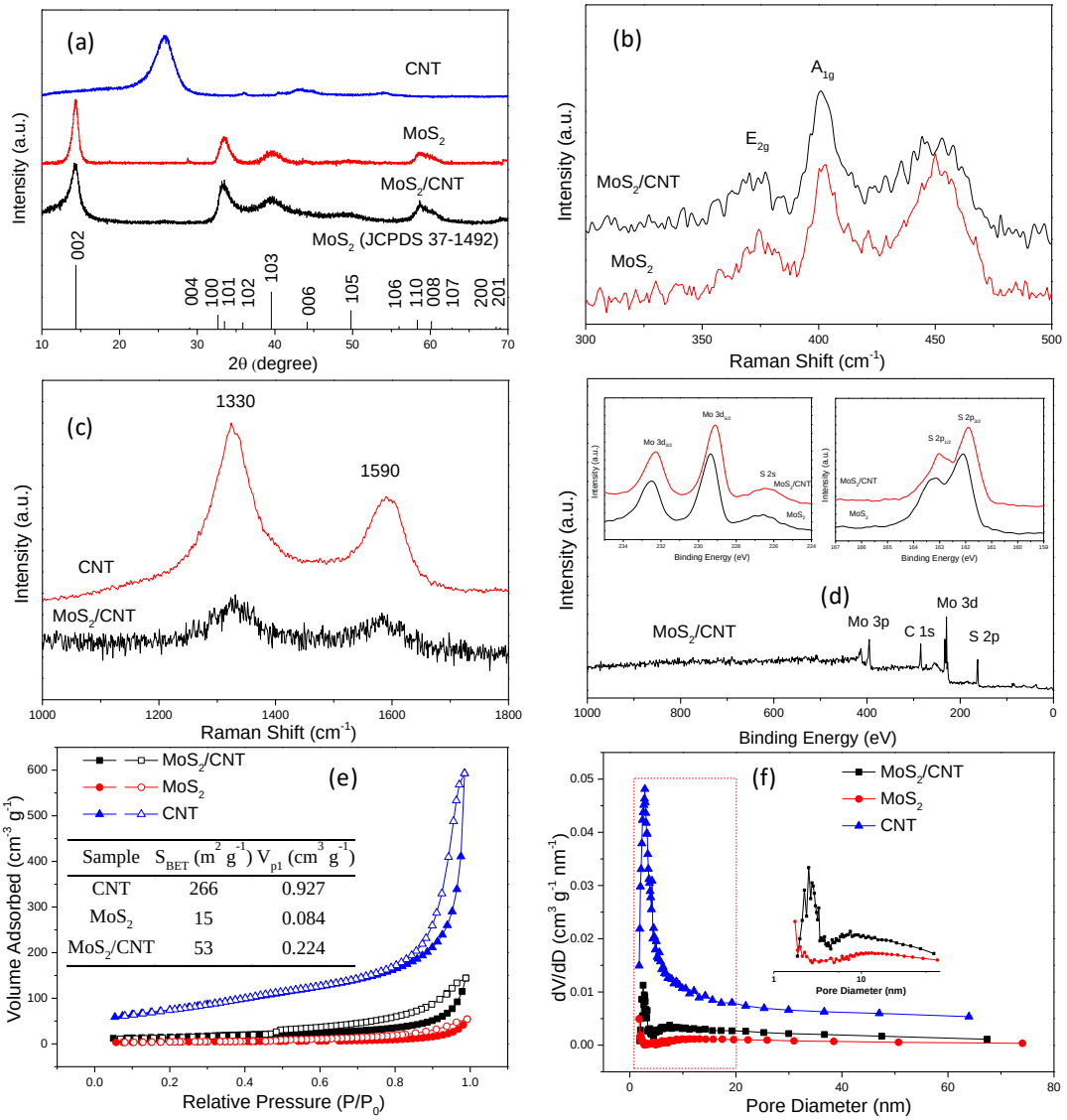

Figure 2.2 (a) XRD patterns, (b-c) Raman spectra, (d) XPS full survey and the corresponding high resolution Mo 3d and S 2p XPS spectra of MoS_2/CNT nanohybrid (insets), (e) Nitrogen adsorption-desorption isotherm and summary of BET surface area and pore volume of all three samples (inset), and (f) the corresponding pore size distribution curves calculated from desorption branch of the nitrogen isotherms (inset showing comparison of MoS_2 and nanohybrid).

The Raman spectrum of MoS_2/CNT reveals typical peaks of the in-plane E^1_{2g} phonon mode (374 cm^{-1}) and out-of-plane A_{1g} vibration phonon mode (402 cm^{-1}) of MoS_2 (Figure 2b), as well as the characteristic peaks of CNT at 1330 cm^{-1} (D band) and 1590 cm^{-1} (G band) (Figure 2.2c), confirming the presence of CNTs in the nanohybrid. According to previous report, the relative integrated intensities between the in-plane and out-of-plane Raman modes provide texture information of MoS_2 thin sheets. A higher intensity of A_{1g} mode than that of E^1_{2g} mode indicates the formation of edge-terminated film, whereas the terrace-terminated MoS_2 has a higher intensity ratio of E^1_{2g} mode than that of A_{1g} mode.[54] Notice that both the pristine MoS_2 and the nanohybrid show consistent edge-terminated spectral features. Therefore, incorporation of CNTs does not change the structure property, which is in good agreement with our XRD observations. In principle, the higher D band intensity is correlated with the larger number of defects in CNTs.[55] The nanohybrid depicts much lower ratio of intensities of D and G bands (I_D/I_G), suggesting that oxygen groups generated during surface functionalization process might be eliminated simultaneously in hydrothermal reaction.[53] Moreover, the diminishing of hydroxyl and carboxyl groups peaks on the infrared (IR) spectrum of nanohybrid is in good agreement with this hypothesis (Figure S1.1).

To gain further insights of the compositions and atomic valence states of the MoS_2/CNT nanohybrid, we conducted X-ray photoelectron spectroscopy (XPS). The overall XPS spectrum (Figure 2.2d, Figure S1.4) exhibits signals of sulfur, molybdenum, and carbon, with barely observable oxygen signal, confirming that the hydroxyl and carboxyl groups introduced by HNO_3 treatment were successfully removed after hydrothermal reaction (Figure S1.1, Figure S1.4),[53, 56, 57] which is favorable for high conductivity in LIB applications.[58] High resolution XPS spectra of Mo 3d and S 2p reveal peaks at 229.1, 232.3, 162.9, and 161.9 eV

(Inset of Figure 2.2d), corresponding to Mo $3d_{3/2}$, Mo $3d_{5/2}$, S $2p_{1/2}$, and S $2p_{3/2}$ components of MoS_2, respectively. Furthermore, the stoichiometric ratio of Mo:S measured from surface layer of both MoS_2 and MoS_2/CNT nanohybrid are close to 1:2, which is in good agreement with the nominal atomic composition of MoS_2 (Figure 2.2d, Figure S1.4).

The nitrogen adsorption-desorption isotherms of all three samples show a type IV with H3-type hysteresis loop, indicating the presence of mesoporous structure (Figure 2.2e). The specific surface area (53 m^2 g^{-1}) and pore volume (0.224 m^3 g^{-1}) of MoS_2/CNT nanohybrid measured using Brunauer–Emmett–Teller (BET) method depict dramatic increase, which is more than 3.5 times higher and 2.6 times greater in comparison with pristine MoS_2 (surface area of 15 m^2 g^{-1} with pore volume of 0.084 m^3 g^{-1}) (inset of Figure 2.2e). Moreover, the pore size distribution of nanohybrid shows a bimodal distribution with a narrow distribution centered at 2.5 nmand a wide distribution centered at 7.5 nm (Figure 2.2f). The smaller pore is associated with CNT and the larger pore is contributed by MoS_2 thin sheets. It should be denoted that pore volume contribution from MoS_2 is much greater than that from CNT, which is consistent with the observation of low CNT concentration. The mesoporous nature of MoS_2/CNT nanohybrid with large surface area is favored in LIB applications since it provides not only large contact area between electrode and electrolyte which reduces the Li ion diffusion pathway, but also provides free space for buffering strains during lithiation/delithiation processes, enabling good rate capability.[50, 59]

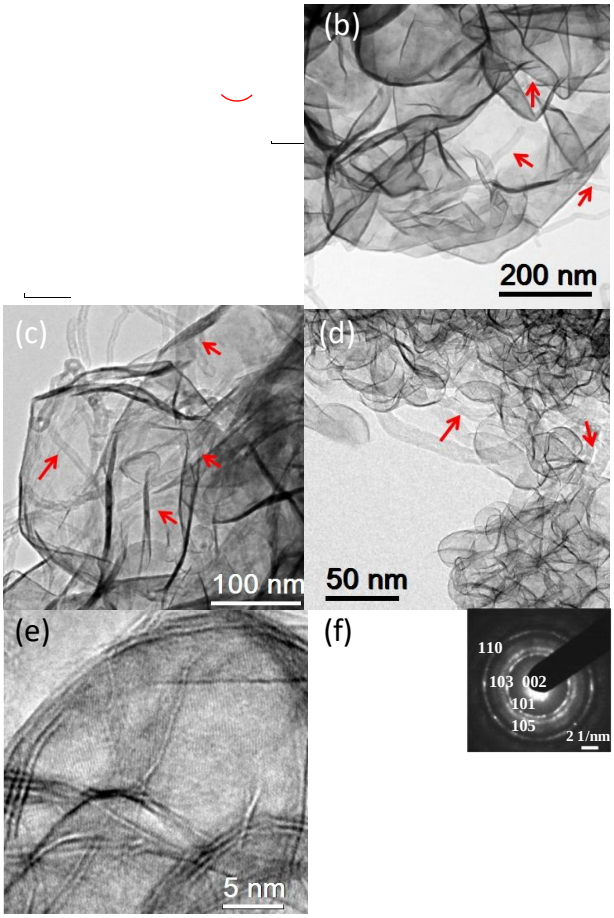

Figure 2.3 HRTEM images of (a) CNT from the nanohybrid. TEM image of (b-d) MoS_2/CNT, and (e-f) HRTEM images of MoS_2/CNT. Insets in (a) and (f) are corresponding SAED patterns.

Further investigation on the morphology and structure of the nanohybrid were obtained by transmission electron microscopy (TEM). A closer view on CNTs demonstrates well maintained structure with a lattice spacing of 0.34 nm corresponding to its (002) plane, which can be observed in the selected area electron diffraction (SAED) pattern (Inset of Figure 2.3a, highlighted by arc). Noticeably, unlike the previous reports,[24, 29-31, 60-62] there is no observable evidence showing MoS_2 growth on CNTs surface in our examinations, which is possibly due to their extremely low concentration and negatively charged surface (Figure S1.5), which is unfavorable for MoO_4^{2-} anions attaching. However, the detailed mechanisms still need

to be further clarified in future work. Figure 3b-d show more evidence of the extreme porous nature of the nanohybrid composed of ultrathin MoS_2 nanosheets supported/separated by CNTs (Marked by red arrows). More specifically, most of the MoS_2 are single layer or two layers, with an average lattice spacing of 0.65 nm (Figure 2.3e-f, Figure S2.2f), which is much larger than the interlayer spacing along z-axis perpendicular to (002) plane of 2H-MoS_2 (JCPDS 37-1492). Kang *et al.* calculated the activation barrier for Li migration in $Li(Ni_{0.5}Mn_{0.5})O_2$ as a function of the Li slab space and found that more interlayer spacing substantially reduces the activation energy for Li motion.[63] A similar conclusion can be drawn here that the enlarged lattice spacing will benefit the Li intercalation/deintercalation, thus further enhance the electrochemical performance in terms of the initial lithiation kinetics and the charge storage capacity.[14, 64] In addition, the SAED pattern clearly identifies a series of well-defined diffraction rings corresponding to the planes of hexagonal-phase MoS_2 (Inset of Figure 2.3f).

To evaluate the electrochemical performance of MoS_2/CNT nanohybrid, the electrode was prepared following practical industrial procedures: mixed with conductor and binder and then coated onto copper foil using automatic thick film coater. The cyclic voltammetry (CV) curves of MoS_2/CNT demonstrate similar patterns like MoS_2 (Figure 2.4a, Figure S1.6a). Upon initial discharge, two prominent reduction peaks were observed at 1.0 V and 0.4 V *vs*. Li/Li^+, respectively. The sharp peak around 1.0 V *vs*. Li/Li^+ is associated the phase transformation in which the coordination of the molybdenum atoms shifts from trigonal prismatic (2H) to octahedral (1T) due to the insertion of lithium ions into the interlayer of the MoS_2.[14, 26] The second peak at approximately 0.4 V has been attributed to a conversion reaction process accompanied by the decomposition of MoS_2 into Mo nanoparticles embedded into a Li_2S matrix and then followed by the formation of solid-electrolyte interphase (SEI) due to the electrolyte

degradation.[26] On the anodic sweep curve, the small oxidation peak at 1.7 V corresponds to the reverse reaction of Mo to MoS_2, and the dominant peak at 2.4 V is associated with the transformation of sulfur (S) from Li_2S in the aforementioned reduction reaction.[14] In the subsequent discharge process, the two peaks at 1.0 V and 0.4 V greatly diminish and a new peak at 1.9 V arises, which is well known in lithium–sulfur battery systems and is associated with the formation of Li_2S.[14] Afterwards, the pertinent redox reaction of MoS_2/CNT nanohybrid involves only lithium and sulfur as the electroactive species.

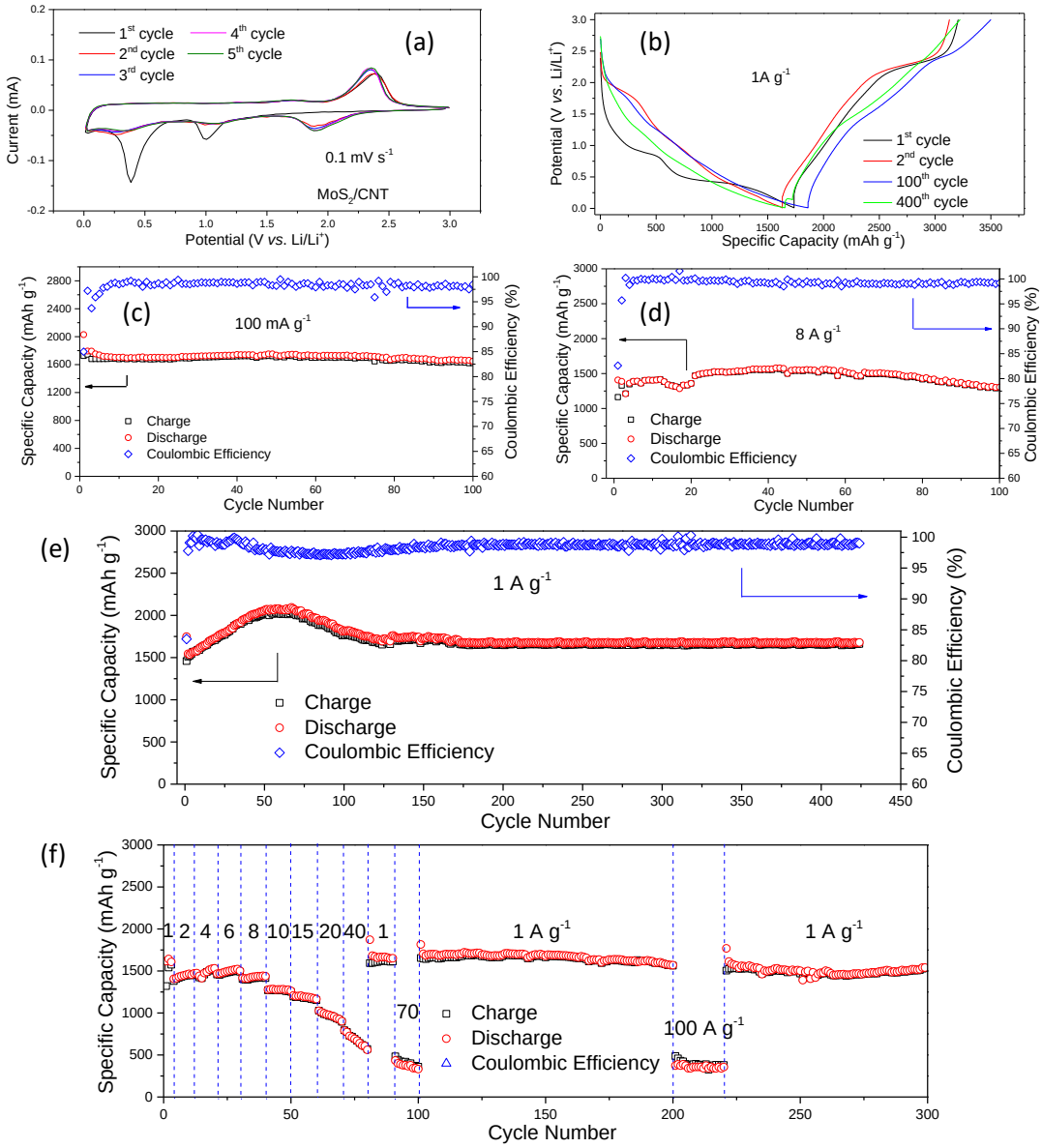

Figure 2.4 CV curves of MoS2/CNT nanohybrid measured in the voltage range of 0.01 - 3.0 V with a scanning rate of 0.1 mV s^{-1}, (b) discharge/charge profiles for the 1st, 2nd, 100th, and 400th cycles at current density of 1 A g^{-1}, (c-e) cycle performance over the same voltage range at the current densities of 100 mA g^{-1}, 8 A g^{-1}, and 1 A g^{-1}, (d) rate capabilities of the nanohybrid.

The voltage profile of MoS_2/CNT nanohybrid clearly depicts two prominent plateaus on the discharge curve and one dominant plateau on the charge curve with inconspicuous reverse reaction process (Mo to MoS_2) (Figure 2.4b). The first discharge and charge capacities are 1747

and 1460 mAh g^{-1}, respectively, corresponding to a Coulombic efficiency of 83.6% (Figure 2.4b, Figure 2.4e). After 425 cycles, it demonstrates as high as 96% discharge capacity (1679 mAh g^{-1}) and 113% charge capacity (1655 mAh g^{-1}) retention of the first cycle. In contrast, pristine MoS_2 suffers severe capacity fading due to the poor electrical conductivity and relatively large particle size (Figure S1.6c). A controlled electrochemical experiment using only CNTs exhibits relatively low capacity even at 100 mAh g^{-1} (Figure S1.6c). Thus it is reasonable to assume that most of the capacity in MoS_2/CNT nanohybrid is contributed by the ultrathin MoS_2 nanosheets. At 1 A g^{-1}, the specific capacity increasing during the initial tens of cycles is presumably due to the high intercalation/deintercalation rate, which was not observed in lower rate cycling (Figure 2.4c). This phenomenon was interpreted by the activation process to facilitate Li^+ ion pathways between the electrolyte and the electrode during cycling.[21] Similar behaviour was found on charge/discharge profiles at 8 A g^{-1} and other high current density tests (Figure 4d, Figure S6e-6g, and Figure S7). At lower current density (100 mA g^{-1}), the nanohybrid shows much higher capacity (1893 mAh g^{-1} in discharge and 1726 mAh g^{-1} in charge) and almost 100% capacity retention within 100 cycles (Figure 2.4c). Even at 8 A g^{-1}, the nanohybrid depicts a discharge capacity of 1305 mAh g^{-1} with no capacity fade even after 100 cycles (Figure 2.4d).

To further evaluate the rate capability, the batteries using MoS_2/CNT nanohybrid as active material were tested under various current densities ranging from 1 A g^{-1} to 100 A g^{-1} (Figure 2.4f, Figure S1.6f). When the current density increase from 2 A g^{-1} to 6 A g^{-1}, the specific capacity shows slight increase, which is consistent with previous observation in cycling test. Upon further increasing of current rate from 8 A g^{-1} to 40 A g^{-1}, the capacity decreases gradually. At 40 A g^{-1}, a discharge capacity as high as 791 mAh g^{-1} is achieved at 71st cycle. When the current density changes back to 1 A g^{-1}, the capacity shows complete recovery and

delivers an even higher discharge capacity (1822 mAh g^{-1}) in the 81st cycle. In addition, the nanohybrid reveals a capacity as high as 505 mAh g^{-1} with discharging/charging rate of 70 A g^{-1}. A charge capacity of 1661 mAh g^{-1} is obtained when the current density restores to 1 A g^{-1} and remains almost 100% for another 100 cycles. Afterwards, the current density is dramatically increased to 100 A g^{-1}, the nanohybrid exhibits a discharge capacity of 500 mAh g^{-1} with proficient stability over 20 cycles. Moreover, when the discharging/charging rate is changed back to 1 A g^{-1}, the specific capacity demonstrates complete recovery and retains for another 100 cycles. Various rate tests starting from 2 A g^{-1} to 100 A g^{-1} depict the same excellent rate capability of as prepared nanohybrid over 400 cycles (Figure S6e-f). The highest rate capacity can be achieved is 512 mAh g^{-1} at 100 A g^{-1} current density, which is approximately 30.5% of the stable discharge capacity at 1 A g^{-1} (Figure S1.6g).

To the best of our knowledge, this is the best rate performance with extremely stable cycle performance for MoS_2-based anode materials (Table S1.1). The results are comparable with or even superior to recently reported state-of-the-art Si or Sn based electrode materials (Table S1.2). The superior rate capability with such stable cycle performance can be attributed to the unique design of the three-dimensionally interconnected CNTs/layered MoS_2 nanohybrid network: a) integrating of high conductive CNTs should not only be able to improve the conductivity, but also keep the structural integrity during continuous charge/discharge processes, leading to stable cycle performance; b) the high surface to volume ratio and ultrathin MoS_2 nanosheets enables extremely short Li ion diffusion pathway further boosting the high power capability; c) it is most likely that the synergy between ultrathin MoS_2 nanosheets and high conductive CNTs plays important role in terms of stabilizing cycle performance and improving specific capacity. It has been reported that combining MoS_2 nanosheets with carbonaceous material, such as graphene,

amorphous carbon, and carbon nanotubes to form a hybrid could integrate the advantages of each individual component that can demonstrate a strong synergistic effect, thus enhancing the intrinsic properties of each component.[65-67]

2.4 Conclusions

In summary, we have successfully demonstrated a rational design of three-dimensionally interconnected carbon nanotube/layered MoS_2 nanohybrid network with best-so-far rate capability and outstanding long-cycle-life. Incorporation of high conductive CNT enhances the electronic conductivity and retains the structural integrity. The monolayer and bilayer MoS_2 ultrathin nanosheets with large surface to volume ratio facilitate fast Li ion transport further boosting high power capability. The nanohybrid delivers discharge capacity as high as 512 mAh g^{-1} at 100 A g^{-1} and 1679 mAh g^{-1} over 425 cycles at 1A g^{-1} with 96% discharge capacity retention of the initial cycle. Therefore, our approach provides a powerful avenue of rational design of simple, low cost and scalable MoS_2/CNT anode materials with high power capability.

CHAPTER 3 HIGHLY DISPERSED Si@C PARTICLES LOADED ON NRGO NANOSHEETS WITH LONG-CYLE-LIFE AND HIGH RATE CAPABILITY FOR LITHIUM ION BATTERIES

3.1 Introduction

Lithium-ion batteries (LIBs) have expanded beyond the traditional use as a power source for portable electronics to electric vehicle (EV) and energy storage in the transportation and energy sectors.[68-72] Conventional LIBs composed of graphite anode and $LiCoO_2$ cathode are unable to meet the increasing demand of higher energy density and long term cycle life.[73] In order to improve the electrochemical performance of rechargeable lithium-ion batteries, tremendous efforts have been devoted to seeking promising alternative electrode materials,[74-77] in which silicon is one of the most promising anode materials due to its extremely high specific capacity (4200 mAh g^{-1}, over ten times state-of-the-art graphite anode).[78-82] However, the successful implementation of Si-based anode in practical LIBs application is seriously hindered by its intrinsic poor electronic conductivity and up to 400% volume expansion/contraction at the fully lithiated state ($Li_{4.4}Si$). The resulting mechanical stress causes cracking and pulverization which destructs and regenerates solid electrolyte interphase (SEI) layer on the fractured surfaces, leading to repaid capacity fading during lithium insertion and extraction.[83, 84] To overcome these drawbacks and stabilize Si-based anode, many solutions have been explored including applying nanostructured Si and carbonaceous coating. To disperse Si nanoparticles homogeneously into a carbonaceous matrix without surface chemical treatment is barely impossible, the fact notwithstanding that most of the existing processes involve manipulation of Si nanopowders as well as air exposure and oxidation of the silicon surface due to carbonization. [81, 83-88]

Herein we present a novel and simple approach to the synthesis of carbon coated Si nanoparticles loaded on graphene nanosheets. Thin layer of carbon shell derived from low cost organic carbon source is coated on highly dispersed Si nanoparticles (NPs) and then loaded on nitrogen doped reduced graphene (NRGO) nanosheets. The gas generation during the carbonization process not only be able to prevent the oxidation of Si NPs but also simultaneously form nitrogen doping on the ultrathin graphene nanosheets. The final Si@C/NRGO nanohybrid has combined merits of the carbon layer coating and NRGO which not only provide volume buffer and improve the conductivity but also isolate the Si particles from direct exposure to electrolyte thus greatly limiting the formation of thick solid electrolyte interpahse (SEI) layer. Hence the nanohybrid demonstrates a superior electrochemical performance which is an ideal candidate for high performance LIBs.

3.2 Experimental Section

3.2.1 Synthesis of Si@C/NRGO

Food grade egg white with no additives was used as the carbon source. In brief, 100 mg Si nanoparticles and 5 g chemically exfoliated graphene oxide (GO) were added into 2 g egg white solution and mixed on a LabRAM Resonant Acoustic mixer (Resodyn, USA) for 30 min. The obtained homogeneous foamy mixture of Si NPs, GO and egg white was heated at 100 ^{o}C for 20 min in oil bath where protein lose its tertiary structure then form cross links, which turns everything solid. The proceeds were collected and dried at 80 ^{o}C in the vacuum oven for eight hours. After drying the foamy structures were directly put in a crucible and heated at 800 °C for 1 hour under continuous Ar with a flow rate of 150 sccm. The heating rate was kept at 5 °C min^{-1}. The composite was washed with HCl and DI water before thoroughly dried to make slurries.

3.2.2 Synthesis of EG-C

The egg white derived carbon (EG-C) sample was prepared following the similar procedures without adding Si nanoparticles. In brief 10 g egg white solution was continuously shaked on a LabRAM Resonant Acoustic mixer for 30 min. The obtained homogeneous foamy mixture was heated at 100 ^{o}C for 20 min in oil bath to perform the cross-linking. The proceeds were collected and dried at 80 ^{o}C in the vacuum oven for eight hours. After drying the foamy structures were directly put in a crucible and heated at 800 °C for 1 hour under continuous Ar with a flow rate of 150 sccm. The heating rate was kept at 5 °C min^{-1}. The composite was washed with HCl and DI water before thoroughly dried to make slurries.

3.2.3 Material Characterization

A Hitachi S-4800 field emission scanning electron microscope (FESEM) and a Hitachi H9000 NAR transmission electron microscope (TEM) operating at an acceleration voltage of 300 KV were used to observe the morphology and structure properties of all samples. Powder X-ray diffraction (XRD) was collected using Bruker D8 Discover A25 diffractometer with copper K_{α} radiation. Raman spectra were taken on a Renishaw 1000B Raman spectrometer with a 632.8 nm HeNe laser source. The elemental compositions of the prepared samples were measured using a CHN analyzer (CE-440, Exeter Analytical Inc., North Chelmsford, MA). Thermogravimetric analysis (TGA) and mass spectrometry were performed on a TA Q50 thermoanalyzer equipped with a Discovery mass spectrometry at heating rate of 5 °C min^{-1} under air/nitrogen condition. The compositions and atomic valence states were carried out on HP 5950A X-ray photoelectron spectroscopy (XPS) with Mg Kα as the source and the C 1s peak at 284.6 eV as an internal standard.

3.2.4 Electrochemical Evaluation

The electrochemical performance was characterized by CR2032-type coin cells, which were assembled in an argon-filled glove box with moisture and oxygen concentrations below 1.0 ppm. Slurry with 80 wt.% of active material, 10 wt.% of Super P conductive carbon black, and 10 wt.% carboxymethyl cellulose (CMC) was coated onto 18 um copper foil following a standard industrial procedure using automatic thick film coater (AFA-IV, MTI Co.). The electrode thickness was controlled to achieve 2 mg cm^{-2} loading. After drying, the electrode foil was cut into 1/4 inch disks as working electrode with 1.0 M $LiPF_6$ in ethylene carbonate/ethyl methyl carbonate (40:60, v/v) as electrolyte and lithium discs as the counter electrode and reference electrode. The charge/discharge tests were performed on a LAND CT2001A (Land, China) battery tester within the voltage range of 0.01 V and 2.0 V. Cyclic voltammetry (CV) and AC impedance were measured on a VersaSTAT 3F (Princeton Applied Research) electrochemical station.

3.3 Results and Discussion

The synthesis of carbon coated Si nanoparticles loaded on graphene nanosheets is illustrated in Figure 3.1a. Firstly a homogeneous foamy mixture of Si NPs, GO, and egg white were obtained by 30 min machine-mixing process using Resodyn™ LabRam resonant mixer (Figure 3.1b-d). Subsequently the obtained mixture was heated at 100 ^{o}C for 20 min in oil bath where protein lost its tertiary structure to form cross links, and then the cross-inked structure turned everything solid which simultaneously locked the Si NPs leaving an extreme porous structure. After drying the collected powders were annealed under Ar flow, during which the protein decomposed to form thin layer of carbon shell on Si surface and the GO was reduced. Due to large amount of reducing gases release (Figure 3.1c) during protein thermal decomposition, oxidation of Si NPs was successfully eliminated meanwhile forming nitrogen

doping in the carbonaceous structure. The final Si@C/NRGO nanohybrid has combined merits of the carbon layer coating and graphene nanosheets which provides volume buffer, improve the conductivity and isolate the Si particles from direct exposure to electrolyte thus greatly limiting the formation of thick solid electrolyte interpahse (SEI) layer. The carbonaceous matrix not only be able to accommodate the volume change, facilitate more efficient electronic/ionic diffusion and provide more active sites but also be able to maintain the electrical contact of the electrode with the current collector and alleviate the large stress developed during continuous charge/discharge cycling. Hence the nanohybrid demonstrates a superior electrochemical performance which is an ideal candidate for high performance LIBs.

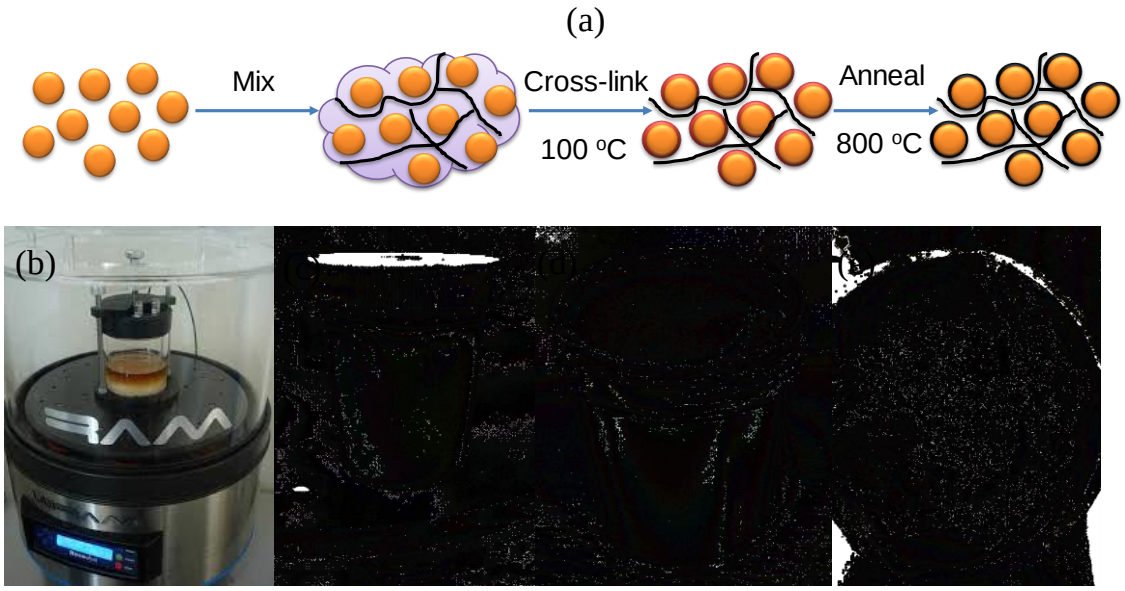

Figure 3.1 Schematic illustration of the preparation process from the precursors to the Si@C/NRGO composite. Digital images of (b) Resodyn™ LabRam resonant mixer, (c-d) foamy structure after 30 minutes mixing, (d) final composite after annealing.

The morphology of these samples was investigated using SEM and TEM. As shown in Figure 3.2a, the pristine Si NPs depict spherical shape with clear surface and an average particle

size of 100 nm. As controlled experiment, Si NPs turns into coarse-textured surface and densely compacted in Si@C composite (Figure 3.2b) due to introducing of EG-C. However, introducing of GO in the synthesis process can greatly increase the porosity of the final hybrid due to the highly-dispersed GO nanosheets provide vital support and separation during the drying and carbonization process, which can dramatically reduce the nanoparticles agglomeration and form unique NRGO nanosheets supported Si@C nanocrystals. A closer observation (Figure 3.2e-f) of the Si@C/NRGO nanohybrid reveals a uniform carbon shell on the Si surface with an average thickness of 8 nm. The high resolution TEM image of Si@C nanoparticle in the Si@C/NRGO nanohybrid (Figure 3.2g) respectively show amorphous carbon layer and lattice fringes with spacing of 0.31 nm which can be ascribed to the (111) plane of Si nanocrystal.

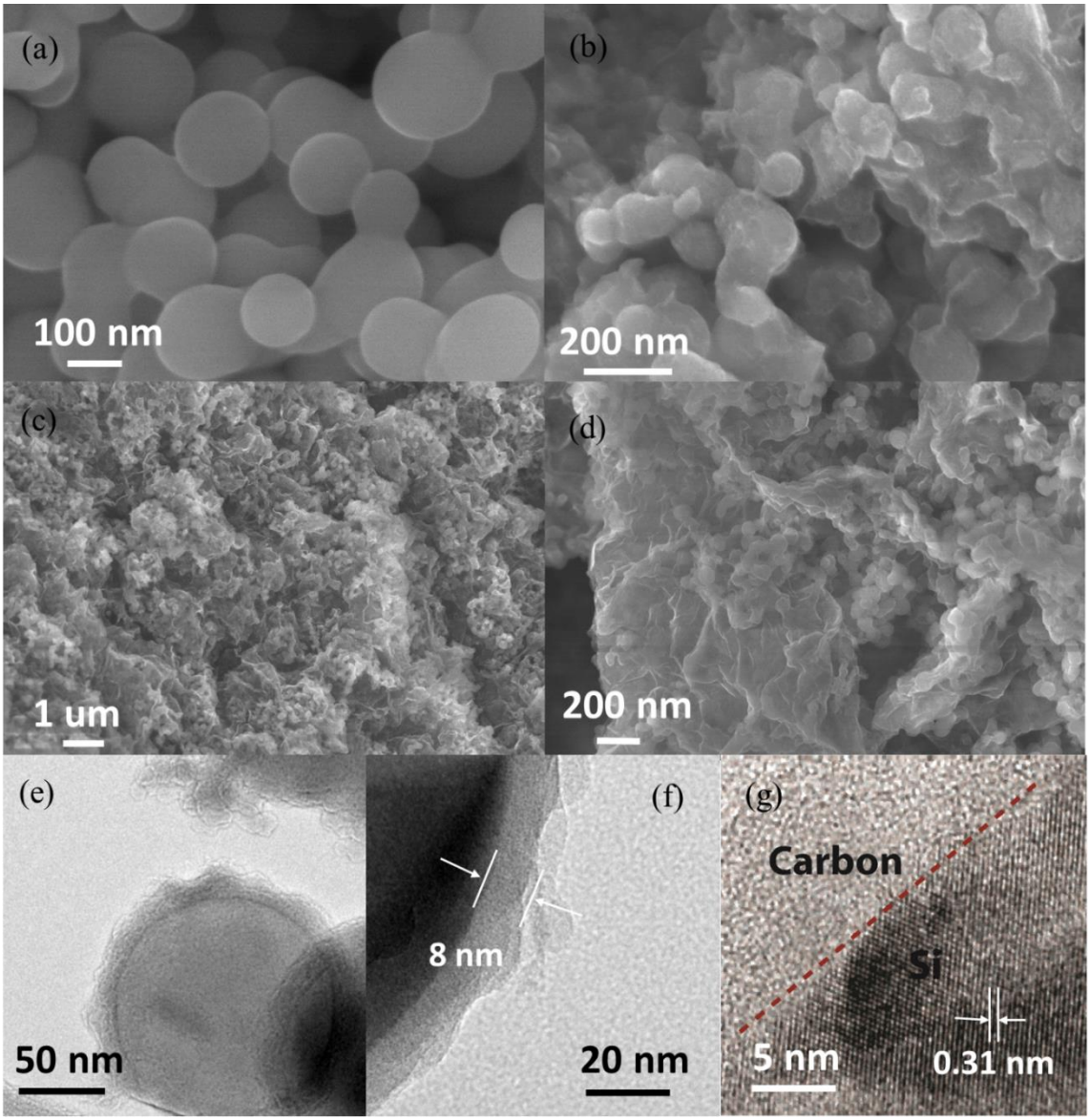

Figure 3.2 FESEM images of (b) pristine Si NPs, (b) Si@C composite, and (c-d) Si@C/NRGO nanohybrid. Low magnification (e-f) and high magnification (g) TEM images of Fe_3C@C/rGO.

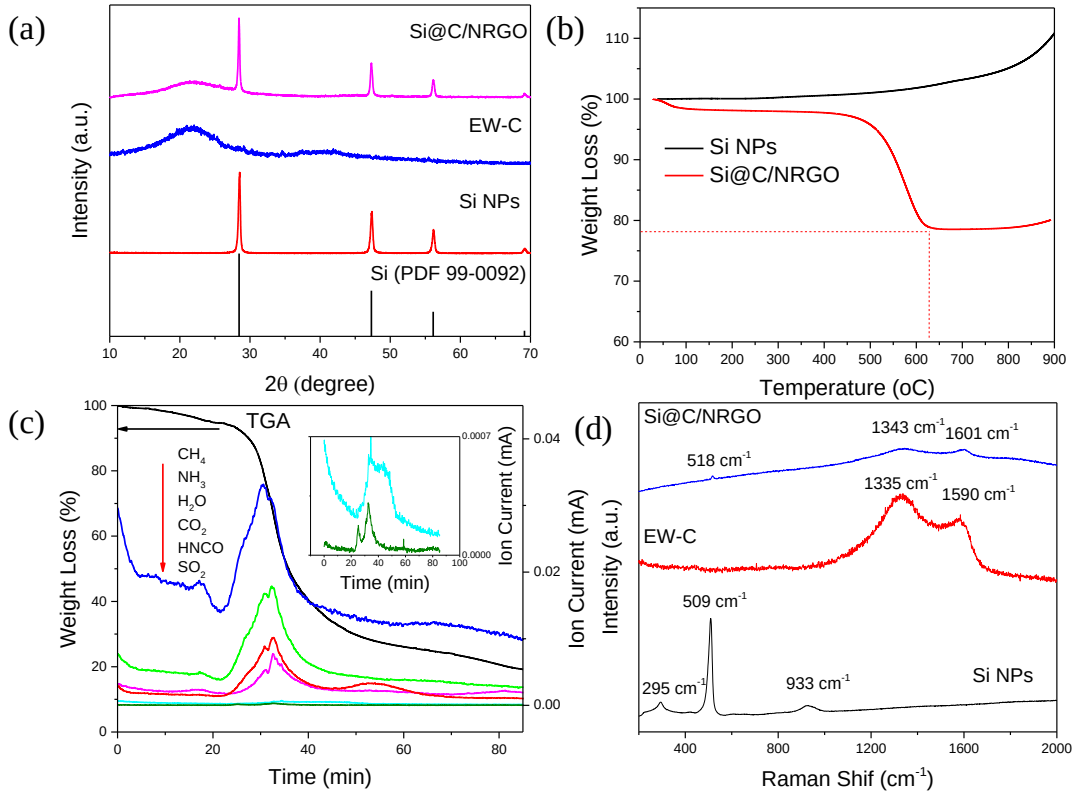

Figure 3.3 (a) XRD patterns, (b) TGA, (c) TGA/MS, and (d) Raman spectra.

The crystal structure and phase information of these materials and were investigated using X-ray diffraction (XRD) (Figure 3.3a). The XRD pattern of EG-C base material exhibits broad peaks around 22^{o} and 41^{o} corresponding to the (002) and (100) peaks of amorphous carbon, which is in agreement with the aforementioned TEM results. On the other hand, the XRD patterns of the pristine Si and Si@C/NRGO composite clearly reveal well-resolved diffraction peaks of crystalline Si (JCPDS, 99-0092), which can be indexed to the (111), (220), (311), (400) and (331) planes of the Si structure. However, the (002) peak is less observable together with an indistinguishable (100) peak in the Si@C/NRGO composite presumably due to the low concentration of amorphous carbon and NRGO, which is further evidenced by the TGA results. In addition, no other characterization peaks from impurities were identified, indicating no

side reactions during the whole process. Thermal gravity analysis (Figure 3.3b) shows that the final hybrid has amorphous carbon and rGO concentration of ~23%, which is very close to the raw material input, showing almost no material loss during the synthesis procedure. Moreover, the exact elemental compositions of all samples were analyzed using CHN analyzer, which reveals that the nanohybrid has C concentration of 22.5%, N concentration of 3.28%, and trace amount of H (0.21%) (Table S2.1). The carbon concentration agrees very well with the TGA analysis. While the N is most likely come from the N doping on the graphene nanosheets and the H is presumably due to the residue of functional groups. As shown in Figure 3c, the combined TGA/MS study clearly shows gas release of CH_4, NH_3, and HNCO during the annealing process, which can not only avoid the oxidation of Si NPs but also forming N doping in graphene nanosheets. Further evidence can be found on the spectrum of X-ray photoelectron spectroscopy (XPS) of the Si@C/NRGO nanohybrid (Figure S2.2). The existence of graphite carbon was confirmed with Raman spectroscopy study. As shown in Figure 3.3d, the Raman spectrum of Si NPS exhibits vibration modes at 295, 509, and 933 cm^{-1}, which correspond to two transverse acoustic phonons (2TA), first order optical phonon (TO) and two transverse optical phonons (2TO) modes of crystalline Si, respectively.[89, 90] Two characteristic peaks corresponding to the D band (~1350 cm^{-1}) and G band (~1590 cm^{-1}) are observed on the Raman spectrum of EG-C sample. In comparison, the Si@C/NRGO composite depicts the TO mode of crystalline Si and the D and G band of carbon together with a significant upshift, shift up of 9, 8 and 11 cm^{-1}, respectively.

To investigate the electrochemical properties of Si@C/NRGO as anode material for LIBs, cyclic voltammogram (CV) measurements were performed in the potential window of 0.01 to 2.0 V at a scan rate of 0.2 mV s^{-1}. As shown in Figure 3.4a, two broad reduction peak between

0.85 and 0.4 V that disappears in subsequent cycles was observed on the first cathodic scan. The former peak could be attributed to the irreversible reduction of electrolyte and the formation of SEI on the electrode surface while the latter probably due to the reaction of lithium ions by oxygen-containing groups on NRGO, which was not found on the CV curve of pristine Si NPs.[91] The existence of oxygen-contain functional group was further evidenced by the XPS observation result (Figure S2.1). The major reduction peak below 0.15 V is ascribed to the lithiation of Si NPs and carbonaceous matrix. On the anodic sweeping two oxidation peaks at 0.35 and 0.53 V can be observed during the delithiation process, related to the phase transformation from amorphous Li_xSi alloy to amorphous Si.[92, 93] The lithiation peak positively shifted to around 0.15 V during the second and subsequent scans, which means the polarization of the Si@C/NRGO decreases after initial cycle activation process. Moreover, it should be noted that the intensity of peak current increases in the initial five cycles due to the gradual activation process. In contrast, the CV curves of pristine Si NPs (and Si@C composite depict the similar pattern other than the overall higher polarization.

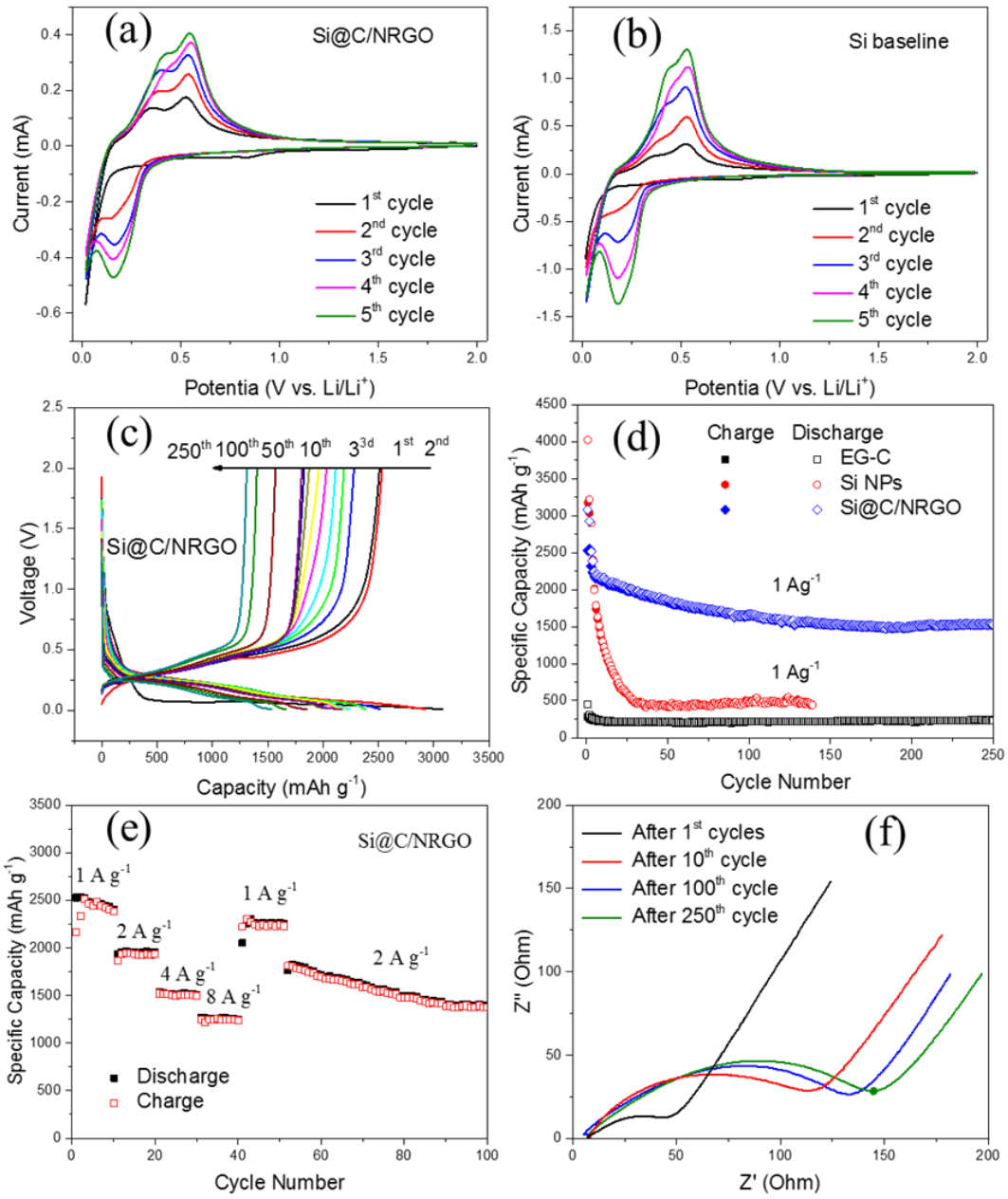

Figure 3.4 (a-b) CV curves of Si@C/NRGO and pristine Si NPs at a scan rate of 0.2 mV s^{-1} between 0.01 and 2.0 V, (c) Voltage profile of Si@C/NRGO and (d) cycle performance of all three samples tested within the same voltage range, (e) Rate performance of Si@C/NRGO nanohybrid and (f) Nyquist plots of in the frequency range between 100 KHz and 100m Hz.

Figure 3.4c displays the discharge/charge curves for the first ten cycles, 50th, 100th and 250th cycle of the Si@C/NRGO nanohybrid electrode. The galvanostatic cycling data were taken at a current density of 100 mA g^{-1} in the first two cycles and 1 A g^{-1} for the rest within a voltage range of 0.01 to 2.0 V. In the first cycle, the nanohybrid delivers discharge/charge capacity of 3079 and 2522 mAh g^{-1}, corresponding to a Coulombic efficiency of 82%. The irreversible capacity loss could be associated with the lithium ion loss due to the formation of solid electrolyte interphase (SEI) and the reaction with aforementioned oxygen-containing functional groups on rGO surface. When the current density increases to 1 A g^{-1} at the 3rd cycle, the Si@C/NRGO nanohybrid exhibits reversible capacity of 2312 mAh g^{-1} with an approximate Coulombic efficiency of 92%. After 250 cycles, a reversible charge capacity of 1525 mAh g^{-1} is retained with a near 99% Coulombic efficiency, close to a 60% capacity retention of the first cycle. As controlled experiment, the cycling performance of pristine Si NPs and EG-C baseline were also evaluated within the same voltage range as shown in Figure 4d. Despite much higher discharge/charge capacity (4020/3174 mAh g^{-1}) in the first cycle, the Si NPs shows much faster capacity fading upon lithiation/delithiation and only 10% of the capacity is retained after less than 140 cycles. On the other side, EG-C reveals typical performance of carbon based anode material with an average capacity of 230 mAh g^{-1}.

Moreover, the Si@C/NRGO nanohybrid demonstrates proficient cyclic stability at various current densities ranging from 1 A g^{-1} to 8 A g^{-1} over 100 cycles. The highest discharge capacity of 2517 mAh g^{-1} is achieved at the 3rd cycle with current density of 1 A g^{-1}. The reversible charge capacities are 1932, 1507, and 1245 mAh g^{-1} for 2, 4, and 8 A g^{-1}, respectively. When the rate returned to 1 A g^{-1} at 41st cycle, the capacity was recovered to as high as 2307 mAh g^{-1} compared with the 2517 mAh g^{-1} recorded for the 3rd 1 A g^{-1} rate cycle,

indicating capacity fading of only 8%. At 46th cycle, the current density is further increased to 2 A g^{-1} and kept for 55 cycles. The nanohybrid delivers a reversible capacity of 1374 mAh g^{-1} at 100th cycle with Coulombic efficiency close to 99%. The remarkably improved electrochemical performance of the Si@C/NRGO nanohybrid in terms of initial cycle Coulombic efficiency and cyclability is presumably due to its unique structural design which employs combinative merits of the immensely dispersed Si NPs and high conductive carbonaceous matrix which not only be able to accommodate the volume change, facilitate more efficient electronic/ionic diffusion and provide more active sites but also be able to maintain the electrical contact of the electrode with the current collector and alleviate the large stress developed during continuous charge/discharge cycling. Thus, a stable SEI layer can be retained, which is supported by the electrochemical impedance spectroscopy (EIS) (Figure 3.4f). The Si@C/NRGO nanohybrid showed dramatic increase of radius in the Nyquist plots from 1st to 10th cycle, indicating a growth of charge transfer resistance due to the SEI formation. But the 100th and 250th are very like the 10th cycle with only a small increase of radius.

3.4 Summary

In conclusion, we have successfully fabricated a novel 3D carbon coated Si NPs loaded on high conductive ultrathin graphene nanosheets for potential use as anode material for high performance LIBs. The unique structural design of Si@C/NRGO has the combined merits of the carbon layer coating and graphene nanosheets which not only provides volume buffer and improve the conductivity but also separates the Si particles from direct exposure to electrolyte to form a stable SEI layer. Thus, the Si@C/NRGO nanohybrid demonstrates a superior electrochemical performance which is an ideal candidate for high performance LIBs. The nanohybrid delivers discharge/charge capacity of 3079 and 2522 mAh g^{-1} in the initial cycle at

100 mA g^{-1}, corresponding to a Coulombic efficiency of 82%. A reversible capacity of 2312 mAh g^{-1} with an approximate Coulombic efficiency of 92% is retained when the current density increases to 1 A g^{-1} at the 3rd cycle. After 250 cycles, the nanohybrid still retains charge capacity of 1525 mAh g^{-1}, close to a 60% capacity retention of the first cycle at 100 mA g^{-1}. Moreover, the Si@C/NRGO nanohybrid demonstrates proficient cyclic stability with reversible capacities of 1932, 1507, and 1245 mAh g^{-1} for 2, 4, and 8 A g^{-1}, respectively.

CHAPTER 4 COUPLED Fe_3C@C NANOCRYSTALS AND REDUCED GRAPHENE OXIDE ELECTROCATALYSTS FOR EFFICIENT OXYGEN REDUCTION REACTION

4.1 Introduction

The searching of advanced nanocatalysts with unprecedented catalytic efficiency at low cost limps toward commercialization of highly efficient fuel cells and lithium-air batteries, whereas the pivotal challenges lie in the kinetically sluggish oxygen reduction reaction (ORR) at the cathode.[33-35] Although Pt-based materials have long been investigated for ORR due to their superior electrocatalytic activity,[35-37] the large-scale application has been hampered due to their high cost, low abundance, low stability, and also the issue of methanol crossover.[38-40] Inspired by the pioneering work on cobalt phthalocyanine (CoPe),[41] numerous efforts have been made to explore alternative catalysts based on non-precious metals (Fe, Co, etc.) [42-44] and metal-free materials [45, 46]. Among them, Fe–N/C complex electrocatalysts have attracted considerable attention as noble-metal-free electrocatalysts for the ORR owing to their low cost and high catalytic activity.[47-49] Despite extensive efforts and rapid progress, it remains a great challenge but desirable to develop porous Fe–carbon nanocatalysts with high surface area for fast mass transport and substantially exposed edge sites for effective catalytic reactions.

Here, we report an economical and scalable one-pot synthetic strategy to prepare ultrathin reduced graphene oxide nanosheets supported edge enriched Fe_3C@C nanocrystals (Fe_3C@C/rGO). The graphene nanosheets provide host and vital support for locally grown Fe_3C nanocrystals, which in-turn perform like separator/spacer to avoid the stacking of ultrathin graphene sheets, leading to an extremely porous Fe_3C@C/rGO architecture with high surface area and super-stable hybrid structure. Such unique structural design of Fe_3C@C/rGO

nanohybrid with large surface area enables fast mass transport and a large number of exposed active edge sites for catalytic reactions. As a result, the nanohybrid exhibits superior electrochemical activity and much-improved stability than commercial Pt/C composite for oxygen reduction reaction.

4.2 Experimental Section

4.2.1 Synthesis of GO

The graphene oxide (GO) was synthesized through chemical exfoliation of graphite powders using a modified Hummers' method.[94] In brief, 1 g of graphite and 0.5 g of potassium nitrate were carefully added into concentrated sulphuric acid which was kept in an ice bath with constant slow stirring. After adding a certain amount of $KMnO_4$, the vigorous solution was then transferred to 40 °C water bath. The whole exfoliation process took about 8 hr under stirring. 8ml 30% H_2O_2 was dropped in the resultant suspension in an ice bath before washing with warm HCl and H_2O, respectively. Graphene oxide powder was prepared by drying the final product at 60 °C in a vacuum oven.

4.2.2 Synthesis of Fe_3C@C/rGO:

In a typical synthesis of Fe_3C@C/rGO, 60 mg of GO from the first step was dissolved in 100 mL of distilled water by continuous ultrasonication for 1 hour to obtain a homogeneous solution. 14 mg $Fe(NO_3)_3 \cdot 9H_2O$ was added to the solution under stirring with constant heating at 80 °C on the hot plate until completely dry. The dark brownish powder was carefully collected and put into a crucible before transferring to a furnace. The temperature was increased to 800 °C with a rate of 5 °C min^{-1} and held at that temperature for 1 hour. The whole heating process was under Ar and CO atmosphere with inflow rate of 150 and 50 sccm, respectively.

4.2.3 Synthesis of Fe_3C@C:

The Fe_3C@C reference catalyst was prepared following the similar procedures without adding GO. In brief, 100 mg $Fe(NO_3)_3 \cdot 9H_2O$ was directly put in a crucible and heated at 800 °C for 1 hour under continuous Ar and Co inflow. The heating rate was kept at 5 °C min^{-1} and inflow rate of Ar and CO atmosphere were 150 and 50 sccm, respectively.

4.2.4 Material Characterization:

A Hitachi S-4800 field emission scanning electron microscope (FESEM) and a Hitachi H9000 NAR transmission electron microscope (TEM) operating at an acceleration voltage of 300 KV were used to observe the morphology and structure properties of all samples. Powder X-ray diffraction (XRD) was collected using Bruker D8 Discover A25 diffractometer with copper K_α radiation. Raman spectra were taken on a Renishaw 1000B Raman spectrometer with a 632.8 nm HeNe laser source. Thermogravimetric analysis (TGA) was performed on a TA SDT 2960 thermoanalyzer with a heating rate of 5 °C min^{-1} under air condition. Surface area was measured by a multipoint BET N_2 adsorption/desorption method (Micromeitrics ASAP200). The compositions and atomic valence states were carried out on HP 5950A X-ray photoelectron spectroscopy (XPS) with Mg Kα as the source and the C 1s peak at 284.6 eV as an internal standard. Zeta potentials were measured in water (pH value ~7) by ZetaPals Zeta Potential Analyzer (BIC, NY).

4.2.5 Electrochemical Measurements:

4.2.5.1 Cyclic voltammetry (CV):

To prepare the working electrodes, 5 mg of certain catalyst, 50 μL Nafion solution (5.0 % Nafion in ethanol) and 450 μL deionized water were mixed by at least 30 min sonication to form homogeneous ink. Then 5 μL suspensions were loaded onto a glass carbon electrode (3mm in

diameter) and fully dried in air. A CH Instruments 600D electrochemical workstation operated in a standard three-electrode configuration was used to conduct the CV tests in 0.1 M KOH electrolyte with various catalysts as the working electrode, a Pt wire as a counter electrode, and an Ag/AgCl electrode as a reference electrode. Prior to CV tests, the electrolyte was bubbled with O_2 or Ar for 30 min and a flow of O_2 or Ar was maintained over the electrolyte during the recording of CVs in order to ensure its continued O_2 or Ar saturation. Nernst equation was used to convert the electrode potential from Ag/AgCl to the reversible hydrogen electrode (RHE) potential:

$$E_{RHE} = E_{Ag/AgCl} + 0.059\ pH + E^{o}_{Ag/AgCl}$$

where E_{RHE} is the converted potential versus RHE, $E_{Ag/AgCl}$ is the measured experimental potential versus the Ag/AgCl reference electrode, and $E^{o}_{Ag/AgCl}$ is the standard potential of Ag/AgCl at 25 °C (0.1976 V).

4.2.5.2 Rotating disk electrode (RDE) measurement:

For the RDE measurement, working electrodes were prepared following the same method as CV's. The polarization curves for ORR were scanned cathodically with a rate of 5 mVs^{-1} at various rotating speed from 400 rpm to 2025 rpm. The number of electrons transferred (n) and kinetic currents (J_k) were calculated using the Koutecky−Levich equation:

$$\frac{1}{J} = \frac{1}{J_L} + \frac{1}{J_K} = \frac{1}{B\omega^{1/2}} + \frac{1}{J_K}$$

Where J is the experimental measured current density, J_K and J_L are the kinetic-limiting and diffusion-limiting current densities, ω is the angular velocity, and B is Levich slope giving by

$$B = 0.62nFC_0{D_0}^{2/3}\nu^{-1/6} \qquad J_K = nFkC_0$$

where n is transferred electron number, F is the Faraday constant (96,500 $C \cdot mol^{-1}$), C_0 is the bulk concentration of O_2 (1.2×10^{-6} mol cm^{-3}), D_0 is the diffusion coefficient of O2 in the electrolyte (1.9×10^{-5} cm s^{-1}), *v* is the kinematic viscosity of the electrolyte (0.01 cm^2 s^{-1}), and k is the electron-transfer rate constant.

4.3 Results and Discussions

The synthetic procedure of Fe_3C@C/rGO nanohybrid is schematically illustrated in Figure 4.1a. In brief, certain amount of iron nitrate was carefully added into homogeneous graphene oxide solution, which was chemically exfoliated using modified Hummers' method.[94] The resulting $Fe(NO_3)_3$@rGO powders after drying at 80 °C were then annealed at 800 °C in co-flow of an argon and carbon monoxide to form a core-shell structured highly porous Fe_3C@C/rGO nanohybrid. During the fabrication process, the ferric ions easily attached to the negatively charged (Figure S3.1) graphene nanosheets surface via the electrostatic interaction. During the annealing process, the graphene nanosheets provide host and vital support for locally grown Fe_3C nanocrystals, which in-turn perform like separator/spacer to avoid the stacking of ultrathin graphene sheets, leading to an extremely porous and super-stable Fe_3C@C/rGO hybrid structure high surface area and enormous exposed edge sites.

Growth of Fe_3C@C nanoparticles on rGO nanosheets was confirmed by scanning electron microscopy (SEM) (Figure 4.4.1b) and Transmission electron microscopy (TEM) (Figure 4.1c-d and Figure S3.2a) observations. The SEM images clearly reveal that well dispersed Fe_3C@C nanocrystals load on the extremely porous graphene sheets. A close view of the TEM observations (Figure 4.1c-e and Figure S3.2b-c) shows Fe_3C nanoparticles averaging of 20 nm well dispersed on highly separated and multi-wrinkled ultrathin graphene nanosheets, which prevent the stacking of rGO nanosheets and dramatically increase the porosity of the final

product. The high resolution TEM images of Fe_3C nanoparticles in the Fe_3C@C/rGO nanohybrid (Figure 4.1e-f and inset) shows lattice fringes with spacing of 0.24 nm (core) and 0.34 nm (shell), which can be ascribed to the (210) plane of Fe_3C (Figure 4.1f) and (002) plane of graphite carbon, respectively. It is worth nothing that only a few layers (mostly around 3 layers) of ultrathin carbon coating are derived on the surface of these Fe_3C nanoparticles but not fully covered (Figure 4.1e, Figure 4.1h, and Figure S3.1b-d), which is favorable for ORR due to extensive exposed edge sites formation (red arrows).[95] Further evidence of the edges formation can be found later by Raman spectroscopy study. Moreover, the corresponding SAED pattern (Figure 4.1g) exhibits the (002), (100), and (110) planes of graphitic carbon and scattered dots from crystalline Fe_3C. In contrast, Fe_3C@C composite (Figure 4.1i-j) shows much bigger particles size (~180 nm) and suffers severe agglomeration. Meanwhile, the carbon layer is much thicker (~60 nm) despite showing similar lattice fringes (Figure 4.1k) and SEAD pattern (inset).

The crystal structure and phase information of Fe_3C@C/rGO and were investigated using X-ray diffraction (XRD) (Figure 4.2a). Both Fe_3C@C and Fe_3C@C/rGO show the characteristic diffraction peaks of Fe_3C species (JCPDS 65-0393). The peak at 26.5^o corresponds to the (002) facets of graphitic carbon (JCPDS 41-1487), indicating the existence of graphite carbon in the composite. While the graphitic carbon peak is less observable on the Fe_3C@C/rGO pattern, which is presumably due to the relatively low rGO concentration and less amount of carbon shell formation, in accordance with aforementioned TEM observations. Thermal gravity analysis (Figure S3.3) shows that the final hybrid has an rGO concentration of ~32%, which is very close to the raw material input, showing almost no material loss during the synthesis procedure. No other impurity was detected on both spectra.

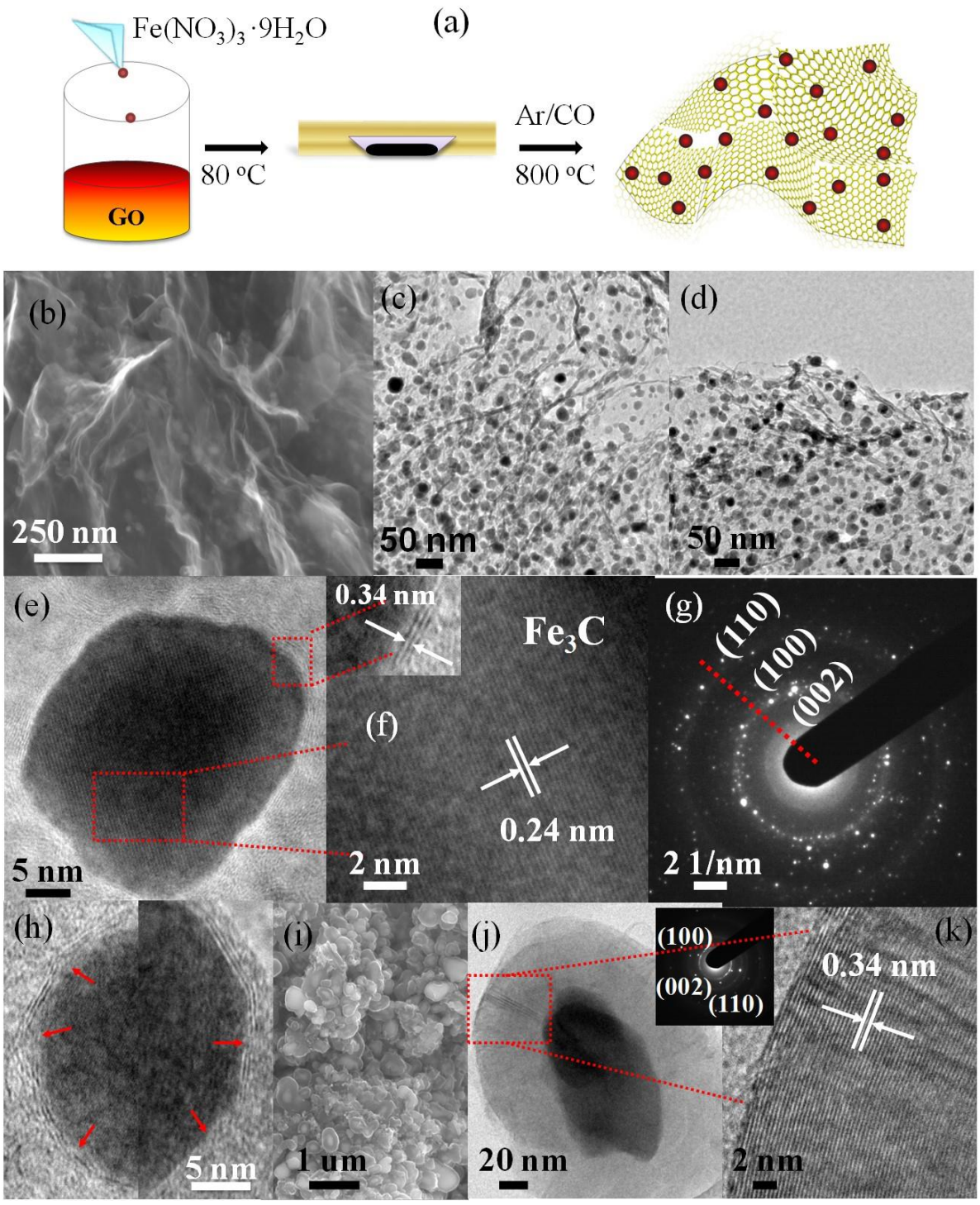

Figure 4.1 (a) Schematic illustration for the synthesis process of Fe_3C@C/rGO. FESEM image (b), low magnification (c-d) and high magnification (e-f and inset) TEM images of Fe_3C@C/rGO. (g) SAED pattern from (e). (h) High magnification TEM image of Fe_3C@C/rGO

and red arrows indicate the edge sites. FESEM image (i) and high magnification (j-k) TEM images of Fe_3C@C. Inset shows the corresponding SAED pattern of (j).

The Raman spectrum of Fe_3C@C composite (Figure 4.2b) clearly reveals the respective D and G band at 1329 and 1582 cm^{-1}, which are corresponded to the disordered graphitic carbon and the E2g vibration of the sp^2-bonded carbon atoms. In comparison, incorporation of graphene nanosheets into the Fe_3C@C/rGO nanohybrid causes slight down shift of both of the D and G bands. More interestingly, the Fe_3C@C/rGO nanohybrid displays more prominent D band with a much higher I_D/I_G ratio, which is possibly due to the formation of discontinuous ultrathin carbon shell leading to more edge structures and much smaller in-plane crystallite sizes [96]. This observation is well consistent with our aforementioned TEM results.

X-ray photoelectron spectroscopy (XPS) measurements were conducted to gain further insights of the compositions and atomic valence states of the Fe_3C@C/rGO nanohybrid. The overall XPS spectrum (inset of Figure 4.2c) exhibits signals of carbon, oxygen, and iron. The high resolution XPS spectra (Figure 4.2c) shows characteristic peaks of Fe $2p_{3/2}$ and Fe $2p_{1/2}$ peaks at 707 and 720 eV, respectively. However, the Fe_3C@C composite shows barely observable iron signal on both of the full and regional spectra probably due to much thicker carbon shell formation, reconfirming our TEM observations, which hinders the signals from Fe_3C nanocrystals.

The nitrogen adsorption/desorption isotherms of Fe_3C@C and Fe_3C@C/RGO show a type IV with H3-type hysteresis loop, indicating the presence of mesoporous structure (Figure 4.2d). The specific surface area of Fe_3C@C/rGO nanohybrid is measured to be 263 $m^2\ g^{-1}$ using Brunauer–Emmett–Teller (BET) method, which is more than 15 times higher in comparison with pristine Fe_3C@C composite (surface area of 17 $m^2\ g^{-1}$) and 1.3 times higher than that of the

commercial Pt/C catalyst (surface area of 201 m^2 g^{-1}, inset of Figure 4.2d), respectively. The dramatically increased surface area is essential for ORR because it not only shortens the diffusion length of reactant and product due to fast mass transport but also provides much more exposed active sites to participate in the ORR process. Thus, it is expected that the Fe_3C@C/rGO nanohybrid will deliver a much higher catalytic activity.

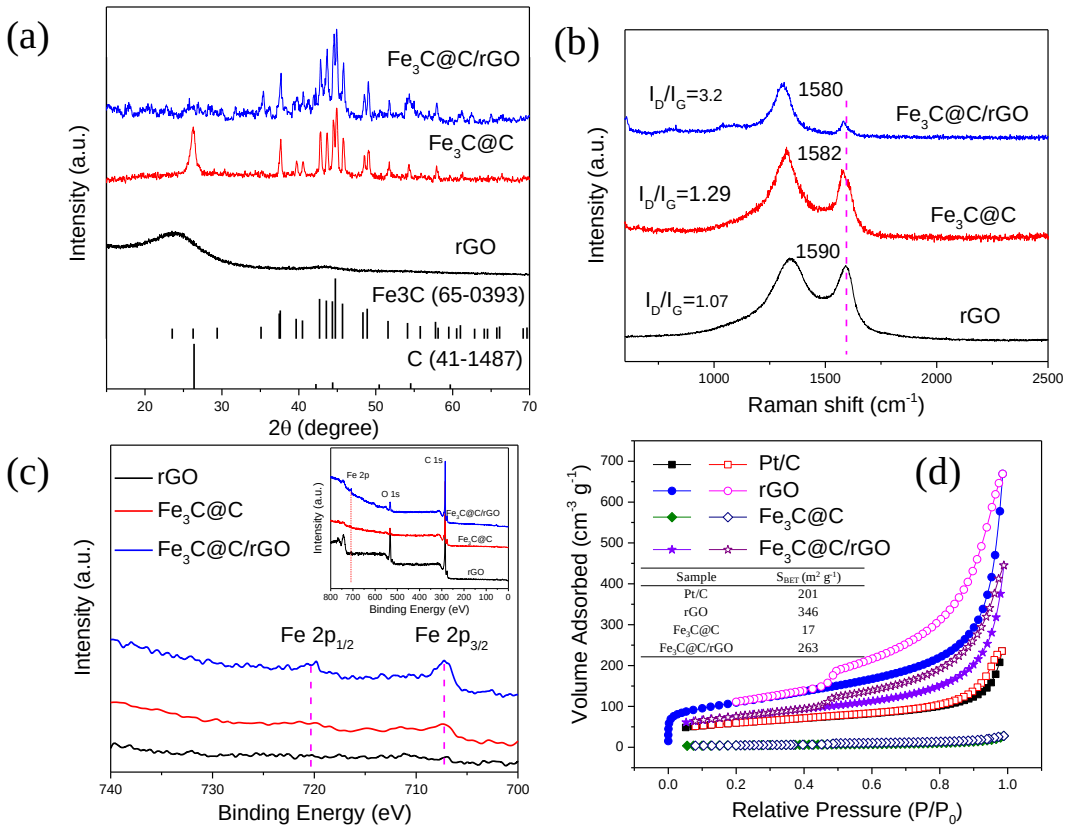

Figure 4.2 (a) XRD patterns, (b) Raman spectra, (c) XPS full survey and the corresponding high resolution Fe2p XPS spectra of Fe_3C@C/rGO nanohybrid (insets), (d) Nitrogen adsorption–desorption isotherm and summary of BET surface area all three samples (inset).

Cyclic voltammograms (CVs) and linear sweep voltammetry (LSV) measurements were performed on a rotating disk electrode (RDE) to evaluate the electrochemical behavior of as prepared catalysts. In brief, 5 mg catalysts were dispersed in 50 μL 5% Nafion and 450 μL deionized water with sonication to achieve a homogeneous suspension. Next, 5.0 μL of the catalyst ink was carefully dropped on the surface of a 3 mm in diameter glassy carbon electrode and dried under an infrared lamp. An O_2 flow was bubbled into the electrolyte (0.1 M KOH solution) for at least 30 min prior to each test. Hereafter, the electrode potential is reported relative to the reversible hydrogen electrode (RHE) potential, which was converted from the Ag/AgCl reference electrode via the Nernst equation: $E_{RHE} = E_{(Ag/AgCl)} + 0.9646$ V [97]. As shown in Figure 4.3a, the rGO or Fe_3C@C alone exhibit very poor ORR activity, with onset potential at 0.8 and 0.88 V, respectively. Remarkably, the Fe_3C@C/rGO nanohybrid presents a much more positive onset potential (~1.0 V) and higher cathodic currents even compared to commercial Pt/C composite, suggesting synergistic ORR catalytic activity of Fe_3C@C and rGO in the hybrid.

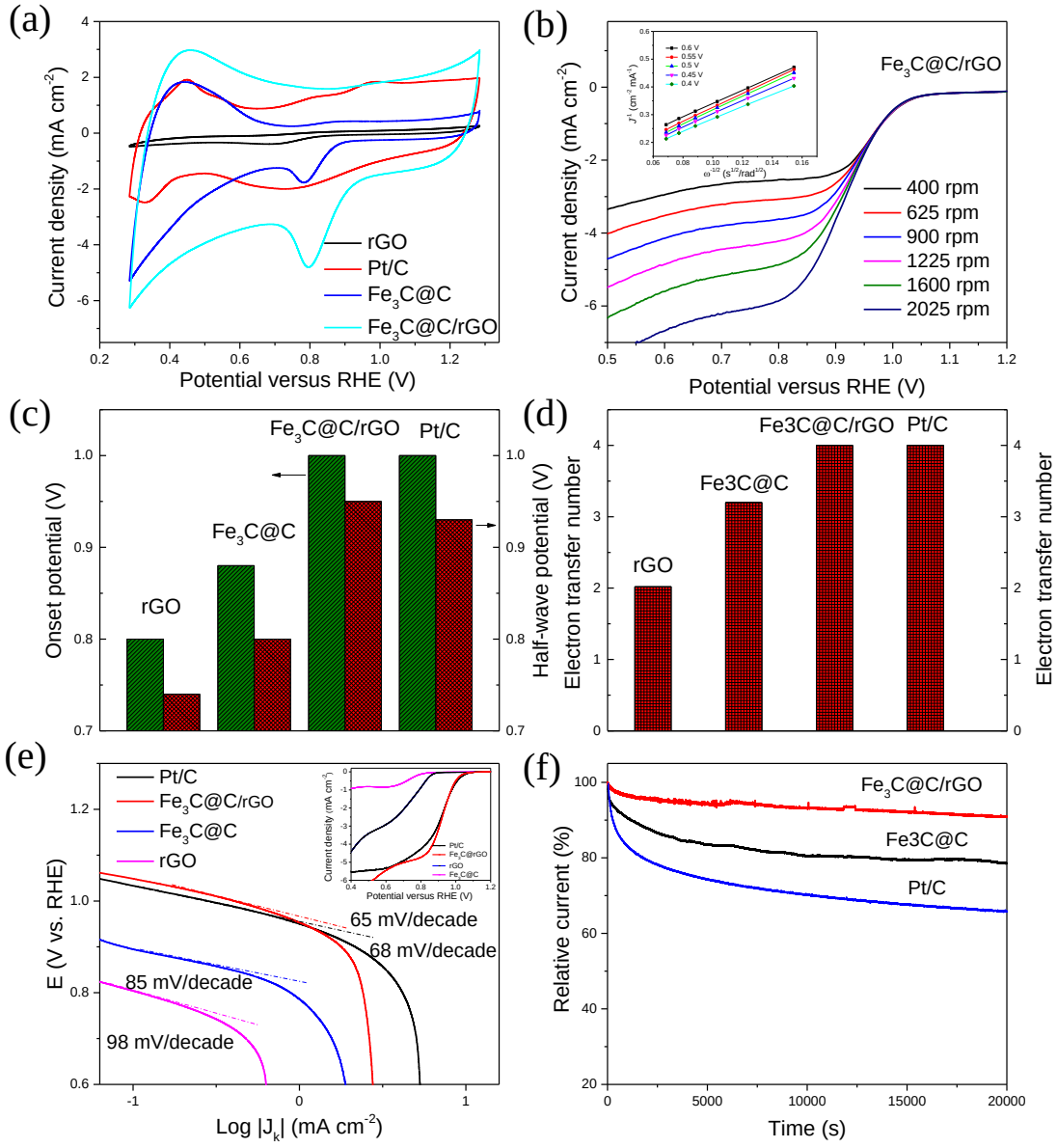

Figure 4.3 (a) CV curves of the rGO, Pt/C, Fe_3C@C, and Fe_3C@C/rGO catalyst in an O_2-saturated 0.1 M KOH solution. (b) Rotating-disk voltammograms of Fe_3C@C/rGO nanohybrid in O_2-saturated 0.1M KOH with a sweep rate of 5mV s^{-1} at various rotation rates indicated (insets are the corresponding K–L plots at different potentials). (c) Onset potentials and half-wave potentials and (d) electron transfer numbers of rGO, Pt/C, Fe_3C@C, and Fe_3C@C/rGO. (e)

The corresponding Tafel plots derived from LSV curves at 1600 rpm (inset). (f) Current–time chronoamperometric response of Pt/C, Fe_3C@C, and Fe_3C@C/rGO.

Linear sweep voltammetry (LSV) measurements were performed on a rotating disk electrode (RDE) to investigate the kinetics of electrocatalytic activity. The current density at the Fe_3C@C/rGO hybrid electrode (Figure 4.3b) increases with increasing rotating speeds as the sequence of the shortened diffusion distance at higher rotational speeds [48]. The great linearity and near parallelism of the fitting lines of the Koutecky-Levich plots (Figure 4.3b inset) indicates first-order reaction kinetics toward the concentration of dissolved oxygen and similar electron transfer numbers for ORR at different potentials [98, 99]. Moreover, the Fe_3C@C/rGO nanohybrid demonstrates a half-wave potential close to 0.95 V, which is 20 mV more positive than the commercial Pt/C composite, indicating much higher electrocatalytic activity toward ORR. The electron transfer number of Fe_3C@C/rGO nanohybrid is almost the same as the Pt/C composite, as shown in Figure 4.3d, which is close to 4.0, revealing a direct four-electron oxygen reduction process for both catalysts. In contrast, the rGO and Fe_3C@C only show electron transfer number of ~2.0 and ~3.2, suggesting a two-electron transfer pathway for rGO and coexisting pathway involving both four-electron and two-step two-electron reduction processes with H_2O_2 as the intermediate agent for Fe_3C@C, respectively. Nevertheless, the current density of Fe_3C@C/rGO nanohybrid at 0.8V is 4.75 mA cm^{-2}, which is much higher than Fe_3C@C and even higher than that of Pt/C composite (4.3 mA cm^{-2}). The improvement of current density can be attributed to the integration of highly porous ultrathin graphene sheets, the enhanced close contact surface, and possible formation of a heterojunction at the interface between Fe_3C@C nanocrystals and rGO sheets, where the high conductive rGO sheets not only act as conduction path for shuttling electrons but also provide extra active ORR sites. Notably, the onset potential

and half-wave potential of Fe_3C@C/rGO nanohybrid are much higher than previously reported materials (Table S3.1), which further proves that superior electrocatalytic activity can achieved through unique structural design.

Furthermore, the Tafel plots (Figure 4.3e) of all four samples were also derived from the mass-transport correction of corresponding RDE data. The Tafel slope of Fe_3C@C/rGO nanohybrid was calculated to be ~ 65 mV/decade, which is even smaller than the Pt/C composite (~ 68 mV/decade), reconfirming the superior catalytic activity for ORR. Notice that this is the smallest Tafel slope reported for Fe_3C based catalysts so far. Moreover, the long-term stability was tested through current–time chronoamperometric response of Pt/C, Fe_3C@C, and Fe_3C@C/rGO. The Pt/C composite catalyst suffered severe current density loss over 20,000 s scan, nearly 34% decrease, which is presumably due to surface oxides and particle dissolution and aggregation in the alkaline electrolytes. Fe_3C@C catalyst showed improved long-term stability, but still has ~22% decay. In comparison, the Fe_3C@C/rGO nanohybrid shows the lowest decay, only ~8% loss of the current density at 0.8 V after 20,000 seconds' continuous operation, suggesting a superior durability for ORR. Such a high catalytic activity and stability of our Fe_3C@C/rGO should benefit from the combined merits of well dispersed ultrathin graphene nanosheets and much smaller edge enriched Fe_3C@C nanocrystals, which are locally grown and crystallized on the surface of graphene sheets, leading to a high surface area and super-stable hybrid structure. Therefore, the loss and agglomeration of the Fe_3C nanocrystals during the durability test are trivial, which may explain the better durability of our catalysts than the Pt/C. As the lack of catalyst durability has been one of the major challenges for alkaline fuel cells, the excellent stability of our Fe_3C@C/rGO nanohybrid makes it promising for ORR and other important catalytic reactions in alkaline solutions.

4.4 Conclusions

In summary, we have successfully demonstrated a superior electrocatalyst composed a 3D extremely porous graphene sheets and edge enriched Fe_3C@C nanocrystals. The graphene nanosheets provide host and vital support for locally grown Fe_3C nanocrystals, which in-turn perform like separator/spacer to avoid the stacking of ultrathin graphene sheets, leading to a high surface area and super-stable Fe_3C@C/rGO hybrid structure. The unique structural design of Fe_3C@C/rGO nanohybrid with large surface area enables fast mass transport and a large number of active sites for catalytic reactions. The Fe_3C@C/rGO nanohybrid exhibits excellent ORR catalytic activity with a high positive onset potential (~1.0 V), a small Tafel slope (65 mV/decade), and excellent durability (only ~8% current density decay at 0.8 V after 20,000 seconds continuous operation), which is superior to that of a commercial Pt/C in an alkaline electrolyte. More importantly, this economical and scalable one-pot synthetic strategy is highly favorable toward practical ORR applications.

CHAPTER 5 CONCLUSION AND RECOMMENDATIONS FOR FUTURE WORK

5.1 Conclusions

Nanostructured materials have offered new opportunities to design high capacity lithium-ion battery anodes and efficient catalysts to replace traditional noble metal such as Pt based materials. The objective of this study is to demonstrate high performance anode with superior rate capacity and long-cycle-life and effective nanocatalyst for oxygen reduction reaction with superior electrocatalytic activity and stability through rational design of novel nanomaterials.

First, a three-dimensionally interconnected carbon nanotube/layered MoS_2 nanohybrid network is reported with best-so-far rate capability and outstanding long cycle life. The monolayer and bilayer MoS_2 ultrathin nanosheets with large surface to volume ratio facilitate fast Li ion transport further boosting high power capability, while incorporating high conductive CNT enhances the electronic conductivity and retains the structural integrity. The nanohybrid delivers discharge capacity as high as 512 mAh g^{-1} at 100 A g^{-1} and 1679 mAh g^{-1} over 425 cycles at 1 A g^{-1} with 96% discharge capacity retention of the initial cycle.

Then a novel 3D carbon coated Si NPs loaded on high conductive ultrathin graphene nanosheets was fabricated for potential use as anode material for high performance LIBs. The unique structural design of Si@C/NRGO has the combined merits of the carbon layer coating and graphene nanosheets which not only provides volume buffer and improve the conductivity but also separates the Si particles from direct exposure to electrolyte to form a stable SEI layer. Thus, the Si@C/NRGO nanohybrid demonstrates a superior electrochemical performance which is an ideal candidate for high performance LIBs. The nanohybrid delivers discharge/charge capacity of 3079 and 2522 mAh g^{-1} in the initial cycle at 100 mA g^{-1}, corresponding to a Coulombic efficiency of 82%. A reversible capacity of 2312 mAh g^{-1} with an approximate

Coulombic efficiency of 92% is retained when the current density increases to 1 A g^{-1} at the 3rd cycle. After 250 cycles, the nanohybrid still retains charge capacity of 1525 mAh g^{-1}, close to a 60% capacity retention of the first cycle at 100 mA g^{-1}. Moreover, the Si@C/NRGO nanohybrid demonstrates proficient cyclic stability with reversible capacities of 1932, 1507, and 1245 mAh g^{-1} for 2, 4, and 8 A g^{-1}, respectively.

Subsequently, a three-dimensionally core-shell structured edge enriched Fe_3C@C nanocrystals on graphene network is demonstrated with superior electrocatalytic activity and stability. The graphene nanosheets provide host and vital support for locally grown edge enriched Fe_3C nanocrystals, which in-turn perform like separator/spacer to avoid the stacking of ultrathin graphene sheets, leading to a high surface area and super-stable Fe_3C@C/rGO hybrid structure. The unique structural design of Fe_3C@C/rGO nanohybrid with large surface area enables fast mass transport and a large number of active sites for catalytic reactions. The Fe_3C@C/rGO nanohybrid exhibits excellent ORR catalytic activity with a high positive onset potential close to 1.0 V, a Tafel slope of 65 mV/decade, and excellent durability with only ~8% current density decay at 0.8 V after 20,000 seconds continuous operation, which is superior to that of a commercial Pt/C in an alkaline electrolyte.

5.2 Recommendations for Future Study

In this thesis, three different novel nanostructures have been demonstrated for high performance anode with superior rate capacity and long-cycle-life and effective nanocatalyst for oxygen reduction reaction with superior electrocatalytic activity and stability through rational design of novel nanomaterials. Overall the electrochemical performance of the engineered materials has been dramatically enhanced compared to the original baseline materials. However, the synthesis processes/methods are still far from satisfaction to meet the practical applications

given many advantages of this category of nanostructures. Therefore, there is plenty of room for discovering the new synthesis methods and optimizing existing procedures towards scale-up phase. Some recommendations for future works are summarized as follows:

- The hydrothermal synthesis of well-separated few layer MoS_2 highly rely on the surface properties of CNTs. However, the existing work did not provide details about the influences of different CNTs on the growth of MoS_2 nanosheets due to the limited availability of variety CNTS in the lab. Extra works can be focused on the fundamental study of detailed mechanism of growth three-dimensionally interconnected carbon nanotube/layered MoS_2 nanohybrid network.
- As a low-cost organic carbon source to the synthesis of 3D carbon coated Si NPs loaded on high conductive ultrathin graphene nanosheets, the MS study clear demonstrated that multiple gases release during the annealing process. Some of the gases are chemically toxic and environmental unfriendly. More works can be done on balancing the cost and electrochemical performance of the Si@C/NRGO nanohybrid.
- A low cost and highly efficient catalyst for oxygen reduction reaction (ORR) is discovered following the Fe_3C@C/rGO work via one-pot annealing approach starting from $Fe(NO_3)_3$ and home use magic foam. The as prepared ultra light carbon foam (ULCF) supported Fe_3C nanoparticle shows extremely porous structure, high surface area, and extraordinary hydrophilic nature. The hybrid electrocatalysts show very high ORR activity compared to Fe_3C@C/rGO nanocomposite. Future work can be done through this direction to further enhance the electrocatalytical performance and reduce the cost.

REFERENCES

[1] Park S, Shao Y, Liu J, Wang Y. Oxygen electrocatalysts for water electrolyzers and reversible fuel cells: status and perspective. Energ Environ Sci. 2012;5(11):9331-44.

[2] Wang Z-L, Xu D, Xu J-J, Zhang X-B. Oxygen electrocatalysts in metal-air batteries: from aqueous to nonaqueous electrolytes. Chemical Society Reviews. 2014;43(22):7746-86.

[3] Winter M, Brodd RJ. What Are Batteries, Fuel Cells, and Supercapacitors? Chemical Reviews. 2004;104(10):4245-70.

[4] Wu H, Chan G, Choi JW, Ryu I, Yao Y, McDowell MT, et al. Stable cycling of double-walled silicon nanotube battery anodes through solid-electrolyte interphase control. Nature Nanotechnology. 2012;7(5):309-14.

[5] Reddy MV, Rao GVS, Chowdari BVR. Metal Oxides and Oxysalts as Anode Materials for Li Ion Batteries. Chemical Reviews. 2013;113(7):5364-457.

[6] Hassoun J, Derrien G, Panero S, Scrosati B. A nanostructured Sn-C composite lithium battery electrode with unique stability and high electrochemical performance. Advanced Materials. 2008;20(16):3169-75.

[7] Li H, Wang Z, Chen L, Huang X. Research on Advanced Materials for Li-ion Batteries. Advanced Materials. 2009;21(45):4593-607.

[8] Wu H, Zheng G, Liu N, Carney TJ, Yang Y, Cui Y. Engineering Empty Space between Si Nanoparticles for Lithium-Ion Battery Anodes. Nano Letters. 2012;12(2):904-9.

[9] Rao CNR, Matte HSSR, Maitra U. Graphene Analogues of Inorganic Layered Materials. Angewandte Chemie-International Edition. 2013;52(50):13162-85.

[10] Stephenson T, Li Z, Olsen B, Mitlin D. Lithium ion battery applications of molybdenum disulfide (MoS2) nanocomposites. Energy & Environmental Science. 2014;7(1):209-31.

[11] Liu Y-T, Zhu X-D, Duan Z-Q, Xie X-M. Flexible and robust MoS2-graphene hybrid paper cross-linked by a polymer ligand: a high-performance anode material for thin film lithium-ion batteries. Chemical Communications. 2013;49(87):10305-7.

[12] Xiao J, Wang X, Yang X-Q, Xun S, Liu G, Koech PK, et al. Electrochemically Induced High Capacity Displacement Reaction of PEO/MoS2/Graphene Nanocomposites with Lithium. Advanced Functional Materials. 2011;21(15):2840-6.

[13] Wang J-Z, Lu L, Lotya M, Coleman JN, Chou S-L, Liu H-K, et al. Development of MoS2-CNT Composite Thin Film from Layered MoS2 for Lithium Batteries. Advanced Energy Materials. 2013;3(6):798-805.

[14] Cao X, Shi Y, Shi W, Rui X, Yan Q, Kong J, et al. Preparation of MoS2-Coated Three-Dimensional Graphene Networks for High-Performance Anode Material in Lithium-Ion Batteries. Small. 2013;9(20):3433-8.

[15] Gong Y, Yang S, Zhan L, Ma L, Vajtai R, Ajayan PM. A Bottom-Up Approach to Build 3D Architectures from Nanosheets for Superior Lithium Storage. Advanced Functional Materials. 2014;24(1):125-30.

[16] Huang G, Chen T, Chen W, Wang Z, Chang K, Ma L, et al. Graphene-Like MoS2/Graphene Composites: Cationic Surfactant-Assisted Hydrothermal Synthesis and Electrochemical Reversible Storage of Lithium. Small. 2013;9(21):3693-703.

[17] Hwang H, Kim H, Cho J. MoS2 Nanoplates Consisting of Disordered Graphene-like Layers for High Rate Lithium Battery Anode Materials. Nano Letters. 2011;11(11):4826-30.

[18] Chang K, Chen W. l-Cysteine-Assisted Synthesis of Layered MoS2/Graphene Composites with Excellent Electrochemical Performances for Lithium Ion Batteries. ACS Nano. 2011;5(6):4720-8.

[19] Zhu C, Mu X, van Aken PA, Yu Y, Maier J. Single-Layered Ultrasmall Nanoplates of MoS2 Embedded in Carbon Nanofibers with Excellent Electrochemical Performance for Lithium and Sodium Storage. Angewandte Chemie-International Edition. 2014;53(8):2152-6.

[20] Ding S, Chen JS, Lou XW. Glucose-Assisted Growth of MoS2 Nanosheets on CNT Backbone for Improved Lithium Storage Properties. Chemistry-a European Journal. 2011;17(47):13142-5.

[21] Zhang L, Lou XW. Hierarchical MoS2 Shells Supported on Carbon Spheres for Highly Reversible Lithium Storage. Chemistry – A European Journal. 2014;20(18):5219-23.

[22] Yang L, Wang S, Mao J, Deng J, Gao Q, Tang Y, et al. Hierarchical MoS2/Polyaniline Nanowires with Excellent Electrochemical Performance for Lithium-Ion Batteries. Advanced Materials. 2013;25(8):1180-4.

[23] Shi Y, Wang Y, Wong JI, Tan AYS, Hsu C-L, Li L-J, et al. Self-assembly of hierarchical MoSx/CNT nanocomposites ($2 < x < 3$): towards high performance anode materials for lithium ion batteries. Scientific Reports. 2013;3.

[24] Wang SY, Zhang LP, Xia ZH, Roy A, Chang DW, Baek JB, et al. BCN Graphene as Efficient Metal-Free Electrocatalyst for the Oxygen Reduction Reaction. Angew Chem Int Edit. 2012;51(17):4209-12.

[25] Park S-K, Yu S-H, Woo S, Quan B, Lee D-C, Kim MK, et al. A simple L-cysteine-assisted method for the growth of MoS2 nanosheets on carbon nanotubes for high-performance lithium ion batteries. Dalton Transactions. 2013;42(7):2399-405.

[26] Wang S, Jiang X, Zheng H, Wu H, Kim S-J, Feng C. Solvothermal Synthesis of MoS2/Carbon Nanotube Composites with Improved Electrochemical Performance for Lithium Ion Batteries. Nanoscience and Nanotechnology Letters. 2012;4(4):378-83.

[27] Wang Q, Li J. Facilitated Lithium Storage in MoS2 Overlayers Supported on Coaxial Carbon Nanotubes. The Journal of Physical Chemistry C. 2007;111(4):1675-82.

[28] Bindumadhavan K, Srivastava SK, Mahanty S. MoS2-MWCNT hybrids as a superior anode in lithium-ion batteries. Chemical Communications. 2013;49(18):1823-5.

[29] GreeleyJ, Stephens IEL, Bondarenko AS, Johansson TP, Hansen HA, Jaramillo TF, et al. Alloys of platinum and early transition metals as oxygen reduction electrocatalysts. Nat Chem. 2009;1(7):552-6.

[30] Snyder J, Fujita T, Chen MW, Erlebacher J. Oxygen reduction in nanoporous metal–ionic liquid composite electrocatalysts. Nat Mater. 2010;9(11):904-7.

[31] Stamenkovic VR, Fowler B, Mun BS, Wang G, Ross PN, Lucas CA, et al. Improved Oxygen Reduction Activity on Pt3Ni(111) via Increased Surface Site Availability. Science. 2007;315(5811):493-7.

[32] Wang D, Xin HL, Hovden R, Wang H, Yu Y, Muller DA, et al. Structurally ordered intermetallic platinum–cobalt core–shell nanoparticles with enhanced activity and stability as oxygen reduction electrocatalysts. Nat Mater. 2013;12(1):81-7.

[33] Wang D, Yu Y, Xin HL, Hovden R, Ercius P, Mundy JA, et al. Tuning Oxygen Reduction Reaction Activity via Controllable Dealloying: A Model Study of Ordered Cu3Pt/C Intermetallic Nanocatalysts. Nano Lett. 2012;12(10):5230-8.

[34] Sun X, Li D, Ding Y, Zhu W, Guo S, Wang ZL, et al. Core/Shell Au/CuPt Nanoparticles and Their Dual Electrocatalysis for Both Reduction and Oxidation Reactions. J Am Chem Soc. 2014;136(15):5745-9.

[35] Morozan A, Jousselme B, Palacin S. Low-platinum and platinum-free catalysts for the oxygen reduction reaction at fuel cell cathodes. Energ Environ Sci. 2011;4(4):1238-54.

[36] Zhou Y, Neyerlin K, Olson TS, Pylypenko S, Bult J, Dinh HN, et al. Enhancement of Pt and Pt-alloy fuel cell catalyst activity and durability via nitrogen-modified carbon supports. Energ Environ Sci. 2010;3(10):1437-46.

[37] Jasinski R. A New Fuel Cell Cathode Catalyst. Nature. 1964;201(4925):1212-3.

[38] Bashyam R, Zelenay P. A class of non-precious metal composite catalysts for fuel cells. Nature. 2006;443(7107):63-6.

[39] Guo S, Zhang S, Wu L, Sun S. Co/CoO Nanoparticles Assembled on Graphene for Electrochemical Reduction of Oxygen. Angewandte Chemie International Edition. 2012;51(47):11770-3.

[40] Shao M-H, Sasaki K, Adzic RR. Pd−Fe Nanoparticles as Electrocatalysts for Oxygen Reduction. J Am Chem Soc. 2006;128(11):3526-7.

[41] Gong K, Du F, Xia Z, Durstock M, Dai L. Nitrogen-Doped Carbon Nanotube Arrays with High Electrocatalytic Activity for Oxygen Reduction. Science. 2009;323(5915):760-4.

[42] Qu L, Liu Y, Baek J-B, Dai L. Nitrogen-Doped Graphene as Efficient Metal-Free Electrocatalyst for Oxygen Reduction in Fuel Cells. Acs Nano. 2010;4(3):1321-6.

[43] Wen Z, Ci S, Zhang F, Feng X, Cui S, Mao S, et al. Nitrogen-Enriched Core-Shell Structured Fe/Fe3C-C Nanorods as Advanced Electrocatalysts for Oxygen Reduction Reaction. Adv Mater. 2012;24(11):1399-404.

[44] Hou Y, Huang T, Wen Z, Mao S, Cui S, Chen J. Metal−Organic Framework-Derived Nitrogen-Doped Core-Shell-Structured Porous Fe/Fe3C@C Nanoboxes Supported on Graphene Sheets for Efficient Oxygen Reduction Reactions. Adv Energy Mater. 2014;4(11):n/a-n/a.

[45] Yang W, Liu X, Yue X, Jia J, Guo S. Bamboo-like Carbon Nanotube/Fe3C Nanoparticle Hybrids and Their Highly Efficient Catalysis for Oxygen Reduction. J Am Chem Soc. 2015;137(4):1436-9.

[46] Liu B, Soares P, Checkles C, Zhao Y, Yu G. Three-Dimensional Hierarchical Ternary Nanostructures for High-Performance Li-Ion Battery Anodes. Nano Letters. 2013;13(7):3414-9.

[47] Wepasnick KA, Smith BA, Schrote KE, Wilson HK, Diegelmann SR, Fairbrother DH. Surface and structural characterization of multi-walled carbon nanotubes following different oxidative treatments. Carbon. 2011;49(1):24-36.

[48] Feng X, Irle S, Witek H, Morokuma K, Vidic R, Borguet E. Sensitivity of Ammonia Interaction with Single-Walled Carbon Nanotube Bundles to the Presence of Defect Sites and Functionalities. Journal of the American Chemical Society. 2005;127(30):10533-8.

[49] Koroteev VO, Bulusheva LG, Asanov IP, Shlyakhova EV, Vyalikh DV, Okotrub AV. Charge Transfer in the MoS2/Carbon Nanotube Composite. The Journal of Physical Chemistry C. 2011;115(43):21199-204.

[50] Kong D, Wang H, Cha JJ, Pasta M, Koski KJ, Yao J, et al. Synthesis of MoS2 and MoSe2 Films with Vertically Aligned Layers. Nano Letters. 2013;13(3):1341-7.

[51] Antunes EF, Lobo AO, Corat EJ, Trava-Airoldi VJ, Martin AA, Veríssimo C. Comparative study of first- and second-order Raman spectra of MWCNT at visible and infrared laser excitation. Carbon. 2006;44(11):2202-11.

[52] Gonçalves AG, Figueiredo JL, Órfão JJM, Pereira MFR. Influence of the surface chemistry of multi-walled carbon nanotubes on their activity as ozonation catalysts. Carbon. 2010;48(15):4369-81.

[53] Datsyuk V, Kalyva M, Papagelis K, Parthenios J, Tasis D, Siokou A, et al. Chemical oxidation of multiwalled carbon nanotubes. Carbon. 2008;46(6):833-40.

[54] Kim YJ, Shin TS, Choi HD, Kwon JH, Chung Y-C, Yoon HG. Electrical conductivity of chemically modified multiwalled carbon nanotube/epoxy composites. Carbon. 2005;43(1):23-30.

[55] Zhou G, Li F, Cheng H-M. Progress in flexible lithium batteries and future prospects. Energy & Environmental Science. 2014;7(4):1307-38.

[56] Shi Y, Wang Y, Wong JI, Tan AYS, Hsu C-L, Li L-J, et al. Self-assembly of hierarchical MoSx/CNT nanocomposites (2<x<3): towards high performance anode materials for lithium ion batteries. Scientific Reports. 2013;3.

[57] Song XC, Zheng YF, Zhao Y, Yin HY. Hydrothennal synthesis and characterization of CNT@MoS2 nanotabes. Materials Letters. 2006;60(19):2346-8.

[58] Yan Y, Ge X, Liu Z, Wang J-Y, Lee J-M, Wang X. Facile synthesis of low crystalline MoS2 nanosheet-coated CNTs for enhanced hydrogen evolution reaction. Nanoscale. 2013;5(17):7768-71.

[59] Kang K, Meng YS, Bréger J, Grey CP, Ceder G. Electrodes with High Power and High Capacity for Rechargeable Lithium Batteries. Science. 2006;311(5763):977-80.

[60] Du G, Guo Z, Wang S, Zeng R, Chen Z, Liu H. Superior stability and high capacity of restacked molybdenum disulfide as anode material for lithium ion batteries. Chemical Communications. 2010;46(7):1106-8.

[61] Chang K, Chen WX. L-Cysteine-Assisted Synthesis of Layered MoS2/Graphene Composites with Excellent Electrochemical Performances for Lithium Ion Batteries. Acs Nano. 2011;5(6):4720-8.

[62] Wang C, Wan W, Huang YH, Chen JT, Zhou HH, Zhang XX. Hierarchical MoS2 nanosheet/active carbon fiber cloth as a binder-free and free-standing anode for lithium-ion batteries. Nanoscale. 2014;6(10):5351-8.

[63] Chang K, Chen WX, Ma L, Li H, Li H, Huang FH, et al. Graphene-like MoS2/amorphous carbon composites with high capacity and excellent stability as anode materials for lithium ion batteries. J Mater Chem. 2011;21(17):6251-7.

[64] Rahman MA, Song GS, Bhatt AI, Wong YC, Wen CE. Nanostructured Silicon Anodes for High-Performance Lithium-Ion Batteries. Advanced Functional Materials. 2016;26(5):647-78.

[65] Piper DM, Evans T, Xu SS, Kim SC, Han SS, Liu KL, et al. Optimized Silicon Electrode Architecture, Interface, and Microgeometry for Next-Generation Lithium-Ion Batteries. Advanced Materials. 2016;28(1):188-+.

[66] Scrosati B, Hassoun J, Sun YK. Lithium-ion batteries. A look into the future. Energy & Environmental Science. 2011;4(9):3287-95.

[67] Hou Y, Li J, Wen Z, Cui S, Yuan C, Chen J. Co3O4 nanoparticles embedded in nitrogen-doped porous carbon dodecahedrons with enhanced electrochemical properties for lithium storage and water splitting. Nano Energy. 2015;12:1-8.

[68] Li J, Hou Y, Gao X, Guan D, Xie Y, Chen J, et al. A three-dimensionally interconnected carbon nanotube/layered MoS2 nanohybrid network for lithium ion battery anode with superior rate capacity and long-cycle-life. Nano Energy. 2015;16:10-8.

[69] McDowell MT, Lee SW, Nix WD, Cui Y. 25th Anniversary Article: Understanding the Lithiation of Silicon and Other Alloying Anodes for Lithium-Ion Batteries. Advanced Materials. 2013;25(36):4966-84.

[70] Hou Y, Li J, Wen Z, Cui S, Yuan C, Chen J. N-doped graphene/porous g-C3N4 nanosheets supported layered-MoS2 hybrid as robust anode materials for lithium-ion batteries. Nano Energy. 2014;8:157-64.

[71] Han H, Song T, Bae JY, Nazar LF, Kim H, Paik U. Nitridated TiO2 hollow nanofibers as an anode material for high power lithium ion batteries. Energy & Environmental Science. 2011;4(11):4532-6.

[72] Landi BJ, Ganter MJ, Cress CD, DiLeo RA, Raffaelle RP. Carbon nanotubes for lithium ion batteries. Energy & Environmental Science. 2009;2(6):638-54.

[73] Song T, Jeon Y, Samal M, Han H, Park H, Ha J, et al. A Ge inverse opal with porous walls as an anode for lithium ion batteries. Energy & Environmental Science. 2012;5(10):9028-33.

[74] Wen ZH, Lu GH, Mao S, Kim H, Cui SM, Yu KH, et al. Silicon nanotube anode for lithium-ion batteries. Electrochemistry Communications. 2013;29:67-70.

[75] Chan CK, Patel RN, O'Connell MJ, Korgel BA, Cui Y. Solution-Grown Silicon Nanowires for Lithium-Ion Battery Anodes. Acs Nano. 2010;4(3):1443-50.

[76] Liu NA, Hu LB, McDowell MT, Jackson A, Cui Y. Prelithiated Silicon Nanowires as an Anode for Lithium Ion Batteries. Acs Nano. 2011;5(8):6487-93.

[77] Luo LL, Yang H, Yan PF, Travis JJ, Lee Y, Liu N, et al. Surface-Coating Regulated Lithiation Kinetics and Degradation in Silicon Nanowires for Lithium Ion Battery. Acs Nano. 2015;9(5):5559-66.

[78] Huang XK, Kim H, Cui SM, Hurley PT, Chen JH. Si-Composite Anode for Lithium-Ion Batteries with High Initial Coulombic Efficiency. Energy Technology. 2013;1(5-6):305-8.

[79] Huang XK, Pu HH, Chang JB, Cui SM, Hallac PB, Jiang JW, et al. Improved Cyclic Performance of Si Anodes for Lithium-Ion Batteries by Forming Intermetallic Interphases

between Si Nanoparticles and Metal Microparticles. Acs Applied Materials & Interfaces. 2013;5(22):11965-70.

[80] Liu X, Zhao HL, Xie JY, Lv PP, Wang K, Cui JJ. SiOx (0 < x <= 2) Based Anode Materials for Lithium-Ion Batteries. Progress in Chemistry. 2015;27(4):336-48.

[81] Chang JB, Huang XK, Zhou GH, Cui SM, Hallac PB, Jiang JW, et al. Multilayered Si Nanoparticle/Reduced Graphene Oxide Hybrid as a High-Performance Lithium-Ion Battery Anode. Advanced Materials. 2014;26(5):758-64.

[82] Cui LF, Yang Y, Hsu CM, Cui Y. Carbon-Silicon Core-Shell Nanowires as High Capacity Electrode for Lithium Ion Batteries. Nano Letters. 2009;9(9):3370-4.

[83] Luo LL, Zhao P, Yang H, Liu BR, Zhang JG, Cui Y, et al. Surface Coating Constraint Induced Self-Discharging of Silicon Nanoparticles as Anodes for Lithium Ion Batteries. Nano Letters. 2015;15(10):7016-22.

[84] Lotfabad EM, Kalisvaart P, Cui K, Kohandehghan A, Kupsta M, Olsen B, et al. ALD TiO2 coated silicon nanowires for lithium ion battery anodes with enhanced cycling stability and coulombic efficiency. Physical Chemistry Chemical Physics. 2013;15(32):13646-57.

[85] Quiroga-Gonzalez E, Carstensen J, Glynn C, O'Dwyer C, Foll H. Pore size modulation in electrochemically etched macroporous p-type silicon monitored by FFT impedance spectroscopy and Raman scattering. Physical Chemistry Chemical Physics. 2014;16(1):255-63.

[86] Yu DP, Bai ZG, Ding Y, Hang QL, Zhang HZ, Wang JJ, et al. Nanoscale silicon wires synthesized using simple physical evaporation. Applied Physics Letters. 1998;72(26):3458-60.

[87] Chang J, Huang X, Zhou G, Cui S, Hallac PB, Jiang J, et al. Multilayered Si Nanoparticle/Reduced Graphene Oxide Hybrid as a High-Performance Lithium-Ion Battery Anode. Advanced Materials. 2014;26(5):758-64.

[88] Yao Y, Liu N, McDowell MT, Pasta M, Cui Y. Improving the cycling stability of silicon nanowire anodes with conducting polymer coatings. Energy & Environmental Science. 2012;5(7):7927-30.

[89] Zhou X, Yin Y-X, Wan L-J, Guo Y-G. Facile synthesis of silicon nanoparticles inserted into graphene sheets as improved anode materials for lithium-ion batteries. Chemical Communications. 2012;48(16):2198-200.

[90] Hummers WS, Offeman RE. Preparation of Graphitic Oxide. J Am Chem Soc. 1958;80(6):1339-.

[91] Shen A, Zou Y, Wang Q, Dryfe RAW, Huang X, Dou S, et al. Oxygen Reduction Reaction in a Droplet on Graphite: Direct Evidence that the Edge Is More Active than the Basal Plane. Angewandte Chemie International Edition. 2014;53(40):10804-8.

[92] Pimenta MA, Dresselhaus G, Dresselhaus MS, Cancado LG, Jorio A, Saito R. Studying disorder in graphite-based systems by Raman spectroscopy. Phys Chem Chem Phys. 2007;9(11):1276-90.

[93] Mao S, Wen Z, Huang T, Hou Y, Chen J. High-performance bi-functional electrocatalysts of 3D crumpled graphene-cobalt oxide nanohybrids for oxygen reduction and evolution reactions. Energ Environ Sci. 2014;7(2):609-16.

[94] Liang Y, Li Y, Wang H, Zhou J, Wang J, Regier T, et al. Co3O4 nanocrystals on graphene as a synergistic catalyst for oxygen reduction reaction. Nat Mater. 2011;10(10):780-6.

[95] Mayrhofer KJJ, Strmcnik D, Blizanac BB, Stamenkovic V, Arenz M, Markovic NM. Measurement of oxygen reduction activities via the rotating disc electrode method: From Pt model surfaces to carbon-supported high surface area catalysts. Electrochim Acta. 2008;53(7):3181-8.

[96] Chang K, Chen W, Ma L, Li H, Li H, Huang F, et al. Graphene-like MoS2/amorphous carbon composites with high capacity and excellent stability as anode materials for lithium ion batteries. Journal of Materials Chemistry. 2011;21(17):6251-7.

[97] Fu K, Yildiz O, Bhanushali H, Wang Y, Stano K, Xue L, et al. Aligned Carbon Nanotube-Silicon Sheets: A Novel Nano-architecture for Flexible Lithium Ion Battery Electrodes. Advanced Materials. 2013;25(36):5109-14.

[98] Kim G, Jeong S, Shin J-H, Cho J, Lee H. 3D Amorphous Silicon on Nanopillar Copper Electrodes as Anodes for High-Rate Lithium-Ion Batteries. Acs Nano. 2014;8(2):1907-12.

[99] Zhu Z, Wang S, Du J, Jin Q, Zhang T, Cheng F, et al. Ultrasmall Sn Nanoparticles Embedded in Nitrogen-Doped Porous Carbon As High-Performance Anode for Lithium-Ion Batteries. Nano Letters. 2014;14(1):153-7.

[100] Nguyen HT, Yao F, Zamfir MR, Biswas C, So KP, Lee YH, et al. Highly Interconnected Si Nanowires for Improved Stability Li-Ion Battery Anodes. Advanced Energy Materials. 2011;1(6):1154-61.

[101] Zhou X, Yin Y-X, Wan L-J, Guo Y-G. Self-Assembled Nanocomposite of Silicon Nanoparticles Encapsulated in Graphene through Electrostatic Attraction for Lithium-Ion Batteries. Adv Energy Mater. 2012;2(9):1086-90.

[102] Qin J, He C, Zhao N, Wang Z, Shi C, Liu E-Z, et al. Graphene Networks Anchored with Sn@Graphene as Lithium Ion Battery Anode. Acs Nano. 2014;8(2):1728-38.

[103] Hwang J, Woo SH, Shim J, Jo C, Lee KT, Lee J. One-Pot Synthesis of Tin-Embedded Carbon/Silica Nanocomposites for Anode Materials in Lithium-Ion Batteries. Acs Nano. 2013;7(2):1036-44.

[104] Xu Y, Liu Q, Zhu Y, Liu Y, Langrock A, Zachariah MR, et al. Uniform Nano-Sn/C Composite Anodes for Lithium Ion Batteries. Nano Letters. 2013;13(2):470-4.

Appendix A Supporting data for Chapter 2

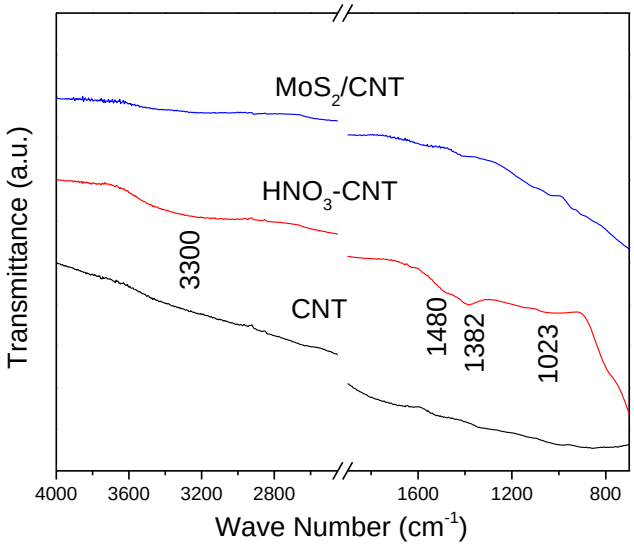

Figure S1.1 FT-IR spectra of pristine CNT, HNO_3 treated CNT, and MoS_2/CNT nanohybrid.

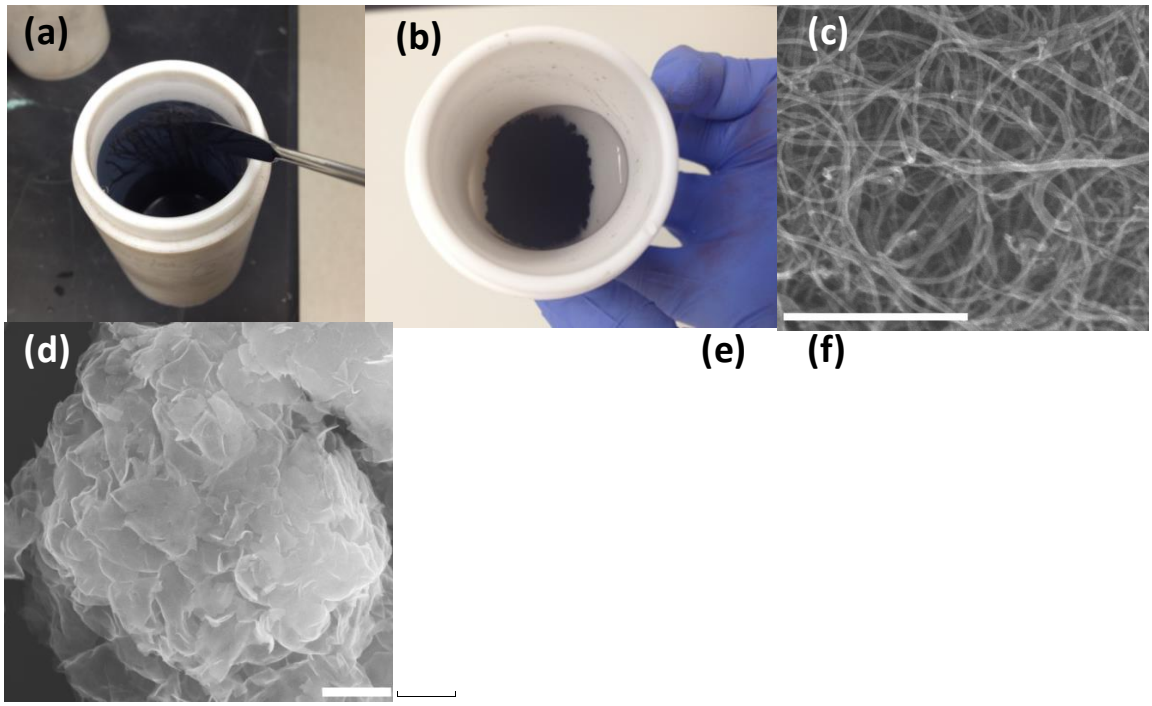

Figure S1.2 Digital images of as prepared (a) MoS_2 and MoS_2/CNT. SEM images (scale bar 500 nm) of (c) CNT and (d) MoS_2. HRTEM images of (e) MoS_2 and (f) MoS_2/CNT nanohybrid.

The concentration of CNTs in the nanohybrid was determined using TGA analysis. All three tests were carried out in air. As shown in Figure S1, MoS_2 starts thermal decomposition to form MoO_3 at around 375 ^oC and reaches equilibrium at around 460 ^oC. The burning temperature of CNT is measured to be 560 ^oC. At 710 ^oC, the sample has a weight loss of 16.58%. By assuming the remaining product is MoO_3 and no Mo atom loss during the TGA analysis, one can calculate the MoS_2 concentration in the original nanohybrid, which is more accurate than by direct comparing weight loss of MoS_2/CNT and MoS_2 (inset, 4.03%). The MoS_2 concentration is estamated to be 93%.

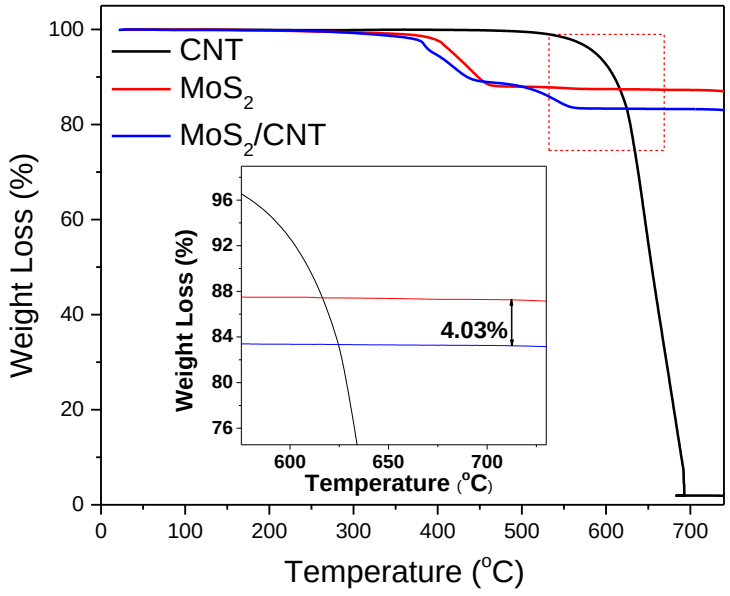

Figure S1.3 TGA curves of CNT, MoS_2, and MoS_2/CNT under flowing air.

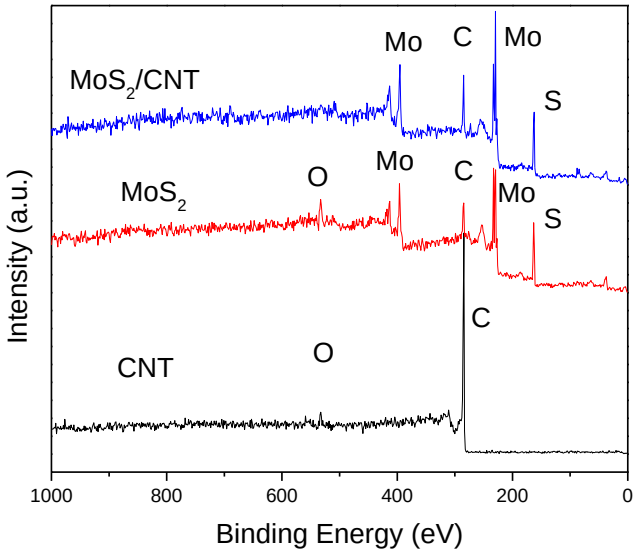

Figure S1.4 XPS surveys of CNT, MoS_2, and MoS_2/CNT (the marked circle showing almost no oxygen existence).

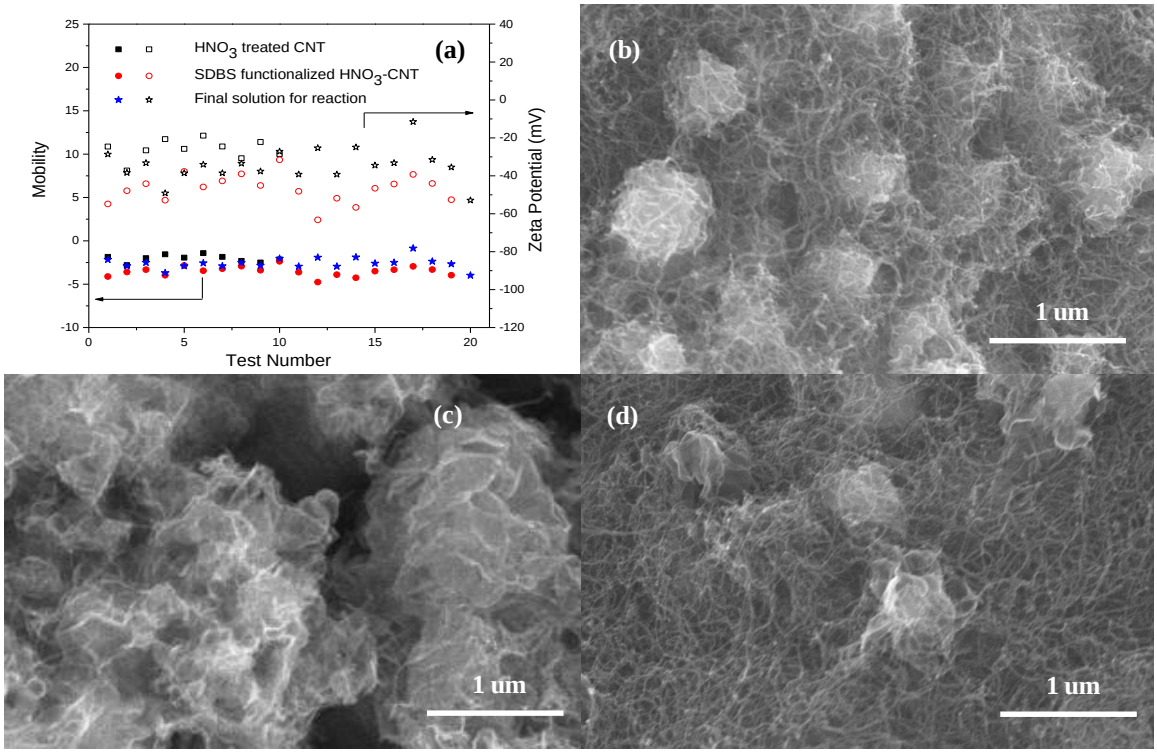

Figure S1.5 (a) Mobility and Zeta potential. SEM images of MoS_2/CNT composites with (b) 60%, (c) 30%, and (d) 10% CNTs input.

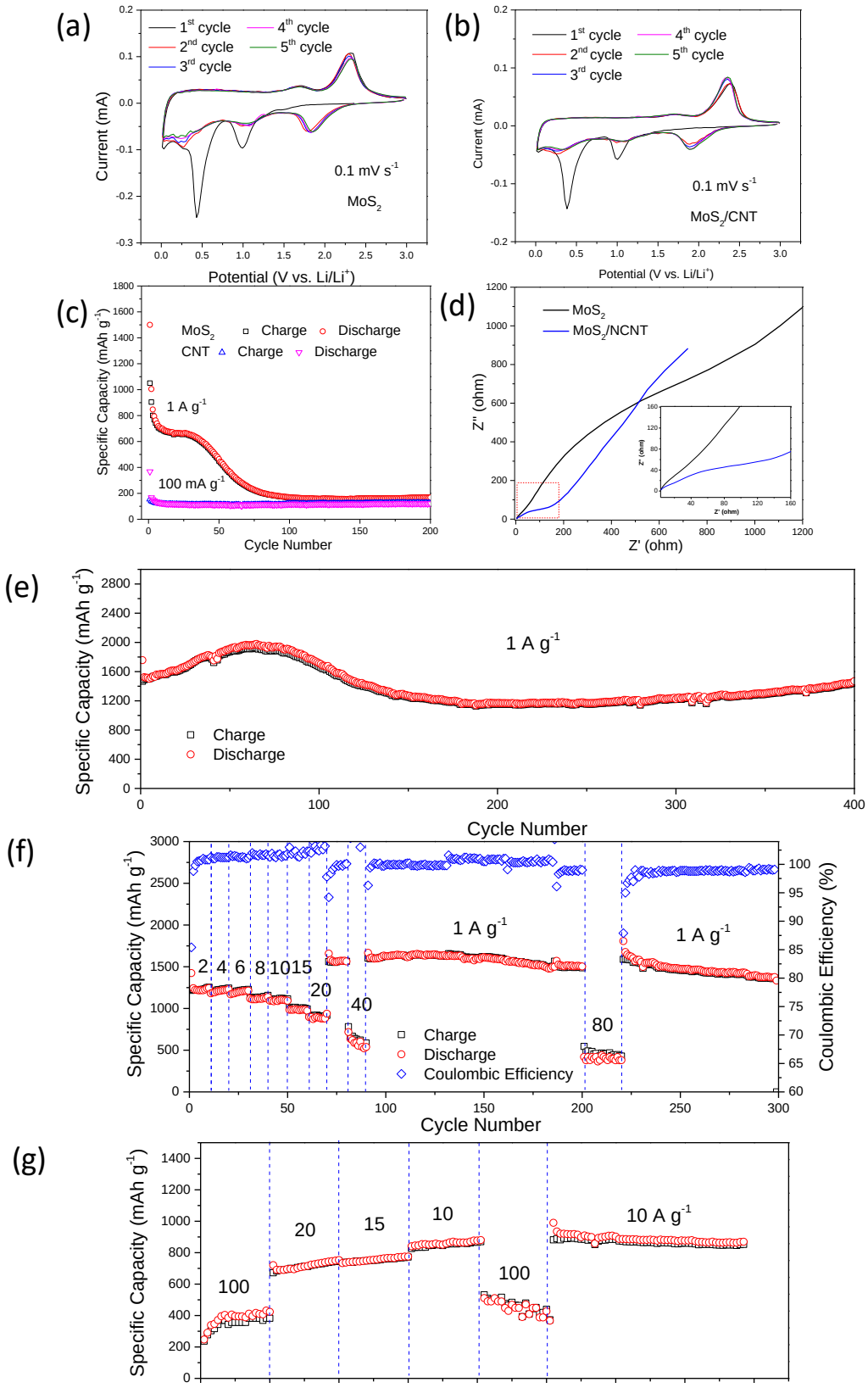
(a)
1st cycle
2nd cycle
3rd cycle
4th cycle
5th cycle
0.1 mV s-1
MoS2
Current (mA)
Potential (V vs. Li/Li+)
(b)
1st cycle
2nd cycle
3rd cycle
4th cycle
5th cycle
0.1 mV s-1
MoS2/CNT
Current (mA)
Potential (V vs. Li/Li+)
(c)
MoS2 Charge Discharge
CNT Charge Discharge
1 A g-1
100 mA g-1
Specific Capacity (mAh g-1)
Cycle Number
(d)
MoS2
MoS2/NCNT
Z'' (ohm)
Z' (ohm)
(e)
1 A g-1
Charge
Discharge
Specific Capacity (mAh g-1)
Cycle Number
(f)
1 A g-1
1 A g-1
2 4 6 8 10 15
20
40
80
Charge
Discharge
Coulombic Efficiency
Specific Capacity (mAh g-1)
Coulombic Efficiency (%)
Cycle Number
(g)
100
20
15
10
100
10 A g-1
Specific Capacity (mAh g-1)

Figure S1.6 CV curves of (a) MoS_2, (b) MoS_2/CNT nanohybrid measured in the voltage range of 0.01 - 3.0 V with a scanning rate of 0.1 mV s^{-1}. (c) Cycling tests of MoS_2 and CNT over 200 cycles at 1 A g^{-1} and 100 mA g^{-1}, respectively. (d) Nyquist plots of pristine MoS_2 and MoS_2/CNT in the frequency range between 100 KHz and 100m Hz. (e) cycle performance of different sample over the same voltage range at the current density of 1 A g^{-1}. (f-g) rate capabilities of the nanohybrid.

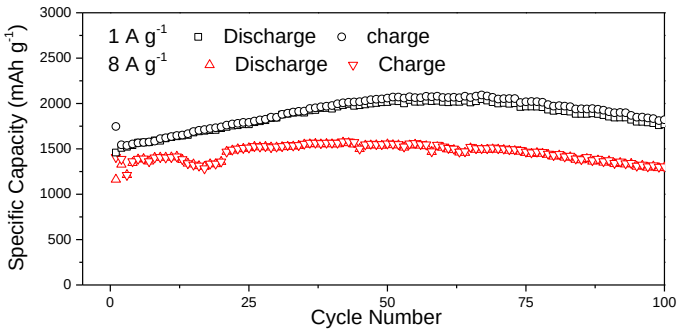

Figure S1.7 Comparison of cycling performance at 1 A g^{-1} and 8 A g^{-1} within the initial 100 cycles.

Table S1.1 Comparison of MoS_2 based anode materials

Active material	Charging rate	Initial cycle coulombic efficiency	Capacity retention (Capacity in mAh g^{-1} / Retention / Cycle No.)	Highest rate capacity in mAh g^{-1} / corresponding current density in A g^{-1}
Our Material	**1 A g^{-1}**	**83.6%**	**1679 / 96% / 425**	**528 / 100**
C_3N_4/NRGO/MoS_2	100 mA g^{-1}	77%	855 / 91% /100	130 / 8
MoS_2[21]	100 mA g^{-1}	83.5%	~900/ NA / 50	554 / 53.1
MoS_2/PNAI Nanowires[26]	100 mA g^{-1}	~72.6%*	952.6 / 90.2% / 50	320 / 1
MoS_2–r-GO–PEO[15]	100 mA g^{-1}	NA	890 / 71% / 100	545 / 2
MoS_2/Graphene (1:2)[22]	100 mA g^{-1}	~65.6%*	~1187 / 103% / 100	~900 / 1
MoS_2/Carbon fiber[23]	1 A g^{-1} 10 A g^{-1}	NA	1007 / NA / 100 661 / NA / 1000	374 / 50
CNT@MoS_2[24]	100 mA g^{-1}	60%	698 / 81% / 60	369 / 1
MoS_2/a-C composites[100]	100 mA g^{-1}	~63%	912 / 95% / 100	961 / 0.1

* Calculated based on the published graph.

Table S1.2 Si and Sn based anode materials

Active material	Charging rate	Initial cycle Coulombic efficiency	Capacity retention (Capacity in mAh g^{-1} / Retention / Cycle No.)	Highest rate capacity in mAh g^{-1} / corresponding current density in A g^{-1}
CNT-Si-C[101]	100 mA g^{-1}	NA	1494 / 94% / 45	1000 / 0.8
Si/graphene/UGF[101]	400 mA g^{-1}	NA	370 / 37.6% /100	NA
a-Si/3D-Cu[102]	1 A g^{-1}	NA	~1600/ NA / 100*	587 / 40
5-Sn/C[103]	0.2 A g^{-1}	~72 %*	~722 / 90.2% / 200	480 / 5
Si NWs[104]	2.1 A g^{-1} 8.4 A g^{-1}	NA	~2930 / 94.5% / 50 ~1800 / 90% / 70	~430 / 33.6
Si-NP@G[105]	100 mA g^{-1}	58.9%*	~1205 / 103% / 150	~990 / 1.6
Sn@G-PGNWs[106]	2 A g^{-1}	NA	657 / 59.7% / 1000	270 / 10
Sn-49-CS[107]	300 mA g^{-1}	NA	440 / 56.4% / 100*	440 / 0.3
Sn-C[108]	200 mA g^{-1}	69%	710 / 69% / 130	~600 / 15.12
Sn@CNT	100 mA g^{-1}		982 / / 100	594 / 5

* Calculated based on the published graph.

Appendix B Supporting data for Chapter 3

Tale S2.1. Elemental composition of Si NPs, EG-C, and Si@C/NRGO.

Sample Name	C	H	N
Si NPs	0.08%	0.02%	0
EG-C	99.26%	0.35%	0.39%
Si@C	22.5%	0.21%	3.28%

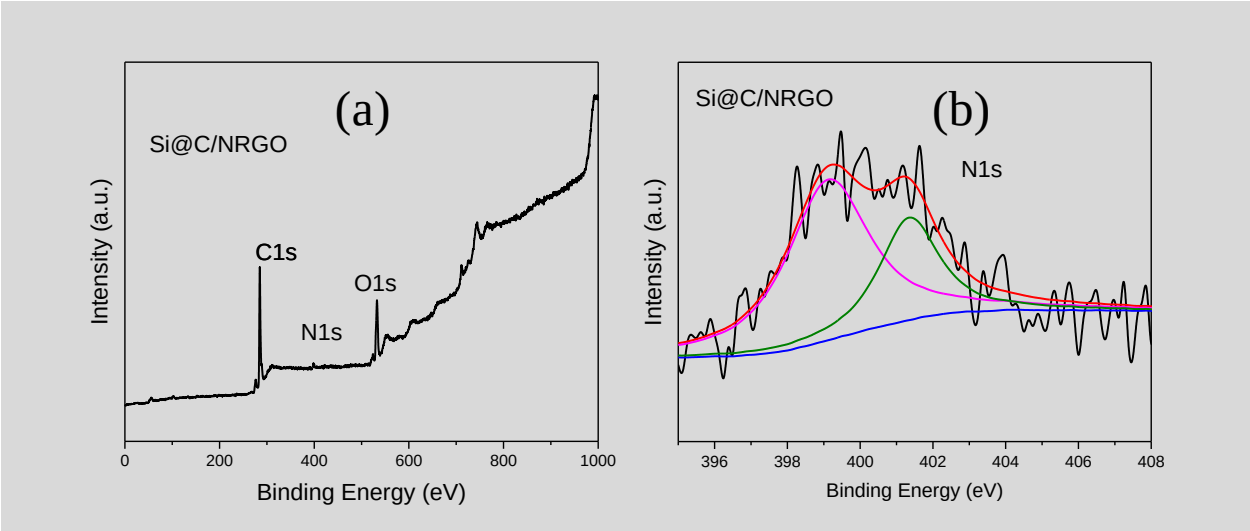

Figure S2.1. (a) XPS full survey and (b) the corresponding high resolution N1s XPS spectrum of Si@C/NRGO nanohybrid.

Appendix C Supporting data for Chapter 4

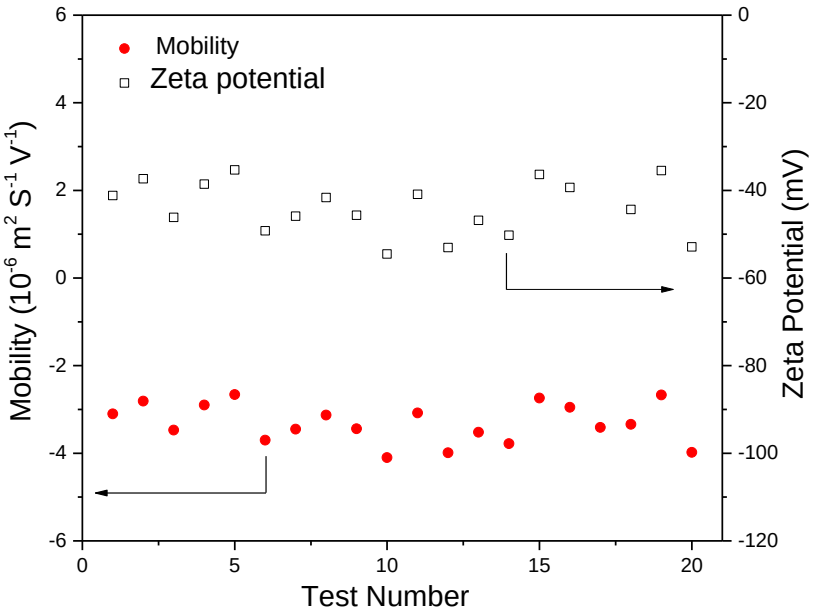

Figure S3.1 Mobility and Zeta potential of Fe_3C@C/rGO nanohybrid.

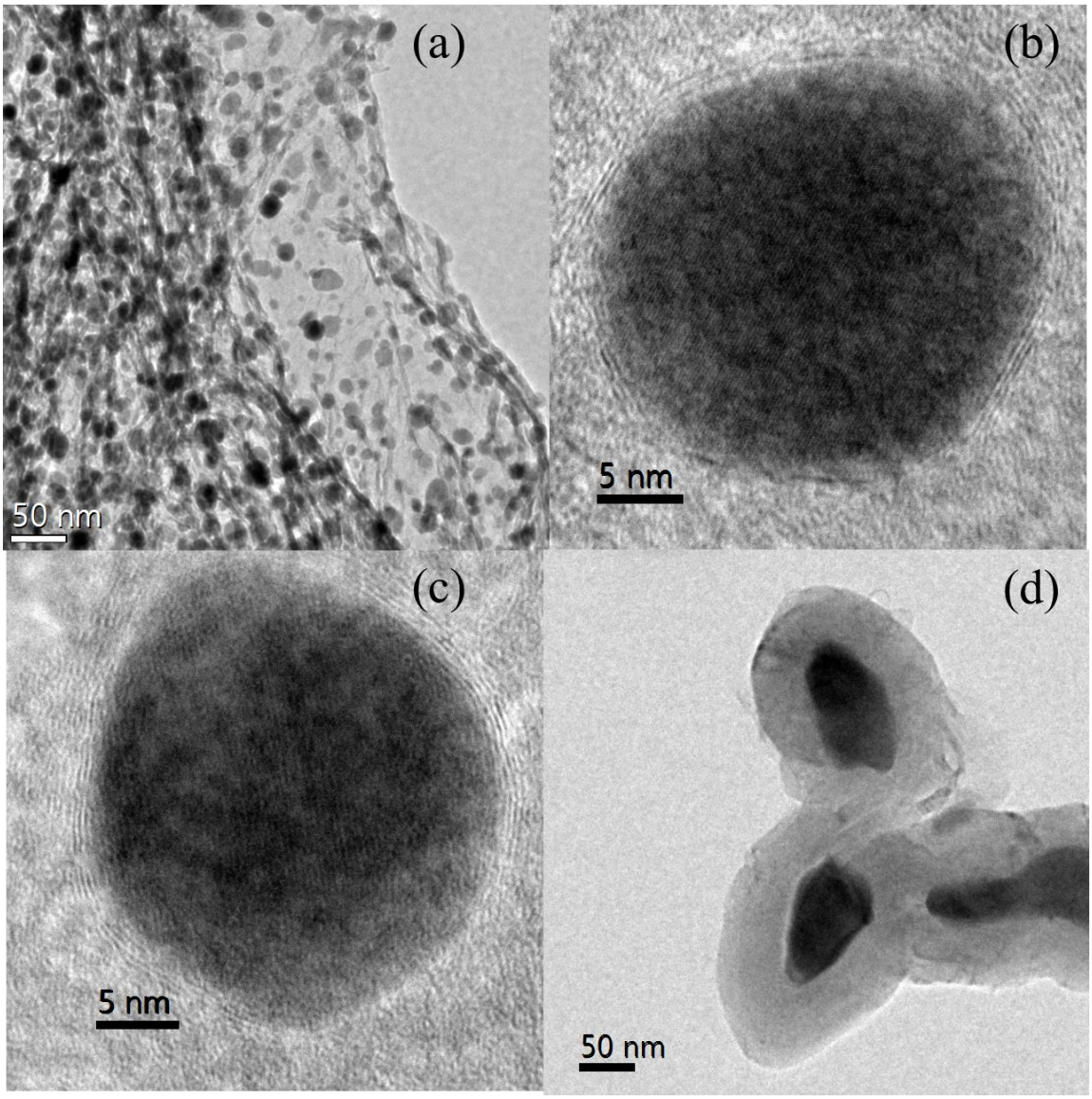

Figure S3.2 TEM images of (a-c) Fe_3C@C/rGO nanohybrid and (d) Fe_3C@C composite.

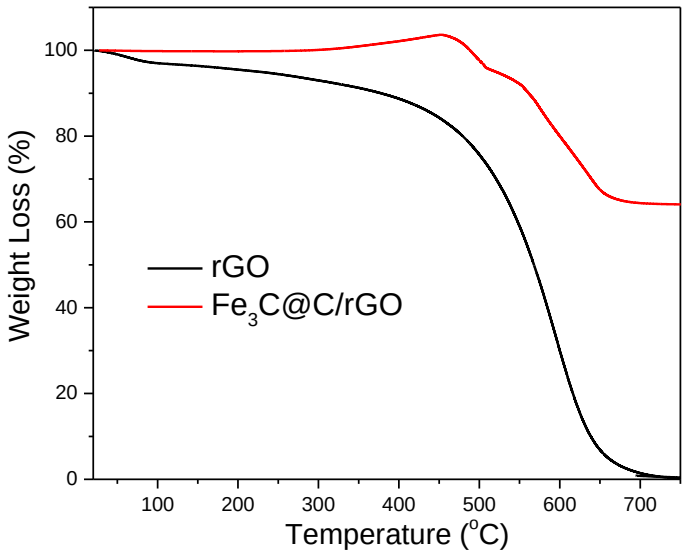

Figure S3.3 TGA curves of rGO and Fe_3C@C/rGO nanohybrid.

To gain the insight information about the Fe_3C@C/rGO nanohybrid composition, TGA analysis was performed on the rGO and our best Fe_3C@C/rGO catalyst (Figure S2.2). When the temperature increases from ~300 ^oC to 455 ^oC, the Fe_3C@C/rGO sample shows slight mass gain which is due to the oxidation of Fe_3C (formation of Fe_2O_3) determined by XRD observation of the TGA residues (Figure S2.3). After reaching to peak at around 455 ^oC , the nanohybrid loses weight continuously until the combustion of all the grahene and carbon shell finish. No further weight loss is observed beyond ~750 ^oC. At 750 ^oC, the sample has a weight loss of 36.5%. From the XRD observation, it is reasonable to assume the remaining product is Fe_2O_3 and no Fe atom loss during the TGA analysis[72]. The Fe_3C concentration is calculated to be ~68% of the original nanohybrid, which is very close the raw material input.

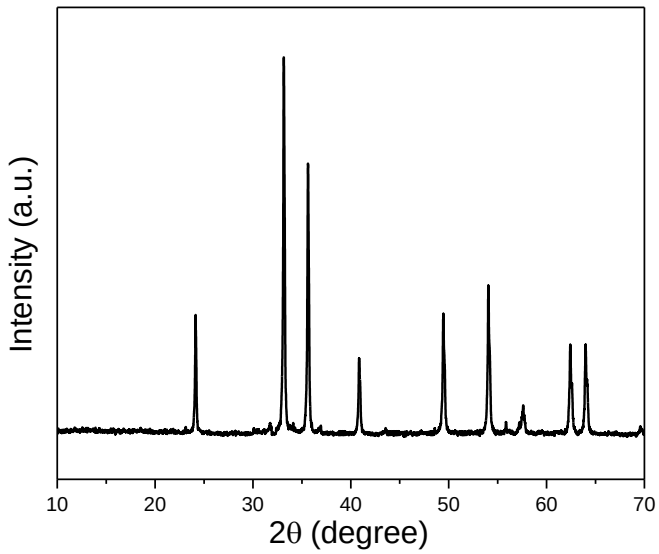

Figure S3.4 XRD pattern of TGA residue of Fe_3C@C/rGO nanohybrid.

CURRICULUM VITAE

Jianyang Li

Place of birth: Heze, Shandong, China

Education:

B. Eng., Southwest University of Science and Technology, China, July 2007
Major: Civil Engineering

M.S., University of Science and Technology of China, China, May 2010
Major: Engineering Mechanics

Ph.D. candidate, Michigan Technological University, May 2010-August 2011
Major: Material Science and Engineering

Ph.D., University of Wisconsin-Milwaukee, expected May 2017
Major: Mechanical Engineering
Dissertation Title: Novel Nanomaterials for Lithium-ion-batteries and Oxygen Reduction Reactions

Research Experiences

Research Assistant, Department of Mechanical Engineering, University of Wisconsin-Milwaukee, Milwaukee, Wisconsin, 2011 – 2016

Energy Engineer, Industrial Assessment Center, University of Wisconsin-Milwaukee, Milwaukee, Wisconsin, 2012 – 2015

Publications (Selected)

[1] Armand M, Tarascon JM. Building better batteries. Nature. 2008;451(7179):652-7.
[2] Zou Z, Ye J, Sayama K, Arakawa H. Direct splitting of water under visible light irradiation with an oxide semiconductor photocatalyst. Nature. 2001;414(6864):625-7.
[3] Armaroli N, Balzani V. The Future of Energy Supply: Challenges and Opportunities. Angewandte Chemie International Edition. 2007;46(1-2):52-66.
[4] Ibrahim H, Ilinca A, Perron J. Energy storage systems—Characteristics and comparisons. Renewable and Sustainable Energy Reviews. 2008;12(5):1221-50.
[5] Park S, Shao Y, Liu J, Wang Y. Oxygen electrocatalysts for water electrolyzers and reversible fuel cells: status and perspective. Energ Environ Sci. 2012;5(11):9331-44.

[6] Wang Z-L, Xu D, Xu J-J, Zhang X-B. Oxygen electrocatalysts in metal-air batteries: from aqueous to nonaqueous electrolytes. Chemical Society Reviews. 2014;43(22):7746-86.
[7] Winter M, Brodd RJ. What Are Batteries, Fuel Cells, and Supercapacitors? Chemical Reviews. 2004;104(10):4245-70.
[8] Wu H, Chan G, Choi JW, Ryu I, Yao Y, McDowell MT, et al. Stable cycling of double-walled silicon nanotube battery anodes through solid-electrolyte interphase control. Nature Nanotechnology. 2012;7(5):309-14.
[9] Reddy MV, Rao GVS, Chowdari BVR. Metal Oxides and Oxysalts as Anode Materials for Li Ion Batteries. Chemical Reviews. 2013;113(7):5364-457.
[10] Hassoun J, Derrien G, Panero S, Scrosati B. A nanostructured Sn-C composite lithium battery electrode with unique stability and high electrochemical performance. Advanced Materials. 2008;20(16):3169-75.
[11] Li H, Wang Z, Chen L, Huang X. Research on Advanced Materials for Li-ion Batteries. Advanced Materials. 2009;21(45):4593-607.
[12] Wu H, Zheng G, Liu N, Carney TJ, Yang Y, Cui Y. Engineering Empty Space between Si Nanoparticles for Lithium-Ion Battery Anodes. Nano Letters. 2012;12(2):904-9.
[13] Rao CNR, Matte HSSR, Maitra U. Graphene Analogues of Inorganic Layered Materials. Angewandte Chemie-International Edition. 2013;52(50):13162-85.
[14] Stephenson T, Li Z, Olsen B, Mitlin D. Lithium ion battery applications of molybdenum disulfide (MoS2) nanocomposites. Energy & Environmental Science. 2014;7(1):209-31.
[15] Liu Y-T, Zhu X-D, Duan Z-Q, Xie X-M. Flexible and robust MoS2-graphene hybrid paper cross-linked by a polymer ligand: a high-performance anode material for thin film lithium-ion batteries. Chemical Communications. 2013;49(87):10305-7.
[16] Xiao J, Wang X, Yang X-Q, Xun S, Liu G, Koech PK, et al. Electrochemically Induced High Capacity Displacement Reaction of PEO/MoS2/Graphene Nanocomposites with Lithium. Advanced Functional Materials. 2011;21(15):2840-6.
[17] Wang J-Z, Lu L, Lotya M, Coleman JN, Chou S-L, Liu H-K, et al. Development of MoS2-CNT Composite Thin Film from Layered MoS2 for Lithium Batteries. Advanced Energy Materials. 2013;3(6):798-805.
[18] Cao X, Shi Y, Shi W, Rui X, Yan Q, Kong J, et al. Preparation of MoS2-Coated Three-Dimensional Graphene Networks for High-Performance Anode Material in Lithium-Ion Batteries. Small. 2013;9(20):3433-8.
[19] Gong Y, Yang S, Zhan L, Ma L, Vajtai R, Ajayan PM. A Bottom-Up Approach to Build 3D Architectures from Nanosheets for Superior Lithium Storage. Advanced Functional Materials. 2014;24(1):125-30.
[20] Huang G, Chen T, Chen W, Wang Z, Chang K, Ma L, et al. Graphene-Like MoS2/Graphene Composites: Cationic Surfactant-Assisted Hydrothermal Synthesis and Electrochemical Reversible Storage of Lithium. Small. 2013;9(21):3693-703.
[21] Hwang H, Kim H, Cho J. MoS2 Nanoplates Consisting of Disordered Graphene-like Layers for High Rate Lithium Battery Anode Materials. Nano Letters. 2011;11(11):4826-30.
[22] Chang K, Chen W. l-Cysteine-Assisted Synthesis of Layered MoS2/Graphene Composites with Excellent Electrochemical Performances for Lithium Ion Batteries. ACS Nano. 2011;5(6):4720-8.
[23] Zhu C, Mu X, van Aken PA, Yu Y, Maier J. Single-Layered Ultrasmall Nanoplates of MoS2 Embedded in Carbon Nanofibers with Excellent Electrochemical Performance for Lithium and Sodium Storage. Angewandte Chemie-International Edition. 2014;53(8):2152-6.
[24] Ding S, Chen JS, Lou XW. Glucose-Assisted Growth of MoS2 Nanosheets on CNT Backbone for Improved Lithium Storage Properties. Chemistry-a European Journal. 2011;17(47):13142-5.
[25] Zhang L, Lou XW. Hierarchical MoS2 Shells Supported on Carbon Spheres for Highly Reversible Lithium Storage. Chemistry – A European Journal. 2014;20(18):5219-23.

[26] Yang L, Wang S, Mao J, Deng J, Gao Q, Tang Y, et al. Hierarchical MoS2/Polyaniline Nanowires with Excellent Electrochemical Performance for Lithium-Ion Batteries. Advanced Materials. 2013;25(8):1180-4.
[27] Shi Y, Wang Y, Wong JI, Tan AYS, Hsu C-L, Li L-J, et al. Self-assembly of hierarchical MoSx/CNT nanocomposites (2 < x < 3): towards high performance anode materials for lithium ion batteries. Scientific Reports. 2013;3.
[28] Wang SY, Zhang LP, Xia ZH, Roy A, Chang DW, Baek JB, et al. BCN Graphene as Efficient Metal-Free Electrocatalyst for the Oxygen Reduction Reaction. Angew Chem Int Edit. 2012;51(17):4209-12.
[29] Park S-K, Yu S-H, Woo S, Quan B, Lee D-C, Kim MK, et al. A simple L-cysteine-assisted method for the growth of MoS2 nanosheets on carbon nanotubes for high-performance lithium ion batteries. Dalton Transactions. 2013;42(7):2399-405.
[30] Wang S, Jiang X, Zheng H, Wu H, Kim S-J, Feng C. Solvothermal Synthesis of MoS2/Carbon Nanotube Composites with Improved Electrochemical Performance for Lithium Ion Batteries. Nanoscience and Nanotechnology Letters. 2012;4(4):378-83.
[31] Wang Q, Li J. Facilitated Lithium Storage in MoS2 Overlayers Supported on Coaxial Carbon Nanotubes. The Journal of Physical Chemistry C. 2007;111(4):1675-82.
[32] Bindumadhavan K, Srivastava SK, Mahanty S. MoS2-MWCNT hybrids as a superior anode in lithium-ion batteries. Chemical Communications. 2013;49(18):1823-5.
[33] GreeleyJ, Stephens IEL, Bondarenko AS, Johansson TP, Hansen HA, Jaramillo TF, et al. Alloys of platinum and early transition metals as oxygen reduction electrocatalysts. Nat Chem. 2009;1(7):552-6.
[34] Snyder J, Fujita T, Chen MW, Erlebacher J. Oxygen reduction in nanoporous metal–ionic liquid composite electrocatalysts. Nat Mater. 2010;9(11):904-7.
[35] Stamenkovic VR, Fowler B, Mun BS, Wang G, Ross PN, Lucas CA, et al. Improved Oxygen Reduction Activity on Pt3Ni(111) via Increased Surface Site Availability. Science. 2007;315(5811):493-7.
[36] Wang D, Xin HL, Hovden R, Wang H, Yu Y, Muller DA, et al. Structurally ordered intermetallic platinum–cobalt core–shell nanoparticles with enhanced activity and stability as oxygen reduction electrocatalysts. Nat Mater. 2013;12(1):81-7.
[37] Wang D, Yu Y, Xin HL, Hovden R, Ercius P, Mundy JA, et al. Tuning Oxygen Reduction Reaction Activity via Controllable Dealloying: A Model Study of Ordered Cu3Pt/C Intermetallic Nanocatalysts. Nano Lett. 2012;12(10):5230-8.
[38] Sun X, Li D, Ding Y, Zhu W, Guo S, Wang ZL, et al. Core/Shell Au/CuPt Nanoparticles and Their Dual Electrocatalysis for Both Reduction and Oxidation Reactions. J Am Chem Soc. 2014;136(15):5745-9.
[39] Morozan A, Jousselme B, Palacin S. Low-platinum and platinum-free catalysts for the oxygen reduction reaction at fuel cell cathodes. Energ Environ Sci. 2011;4(4):1238-54.
[40] Zhou Y, Neyerlin K, Olson TS, Pylypenko S, Bult J, Dinh HN, et al. Enhancement of Pt and Pt-alloy fuel cell catalyst activity and durability via nitrogen-modified carbon supports. Energ Environ Sci. 2010;3(10):1437-46.
[41] Jasinski R. A New Fuel Cell Cathode Catalyst. Nature. 1964;201(4925):1212-3.
[42] Bashyam R, Zelenay P. A class of non-precious metal composite catalysts for fuel cells. Nature. 2006;443(7107):63-6.
[43] Guo S, Zhang S, Wu L, Sun S. Co/CoO Nanoparticles Assembled on Graphene for Electrochemical Reduction of Oxygen. Angewandte Chemie International Edition. 2012;51(47):11770-3.
[44] Shao M-H, Sasaki K, Adzic RR. Pd−Fe Nanoparticles as Electrocatalysts for Oxygen Reduction. J Am Chem Soc. 2006;128(11):3526-7.
[45] Gong K, Du F, Xia Z, Durstock M, Dai L. Nitrogen-Doped Carbon Nanotube Arrays with High Electrocatalytic Activity for Oxygen Reduction. Science. 2009;323(5915):760-4.
[46] Qu L, Liu Y, Baek J-B, Dai L. Nitrogen-Doped Graphene as Efficient Metal-Free Electrocatalyst for Oxygen Reduction in Fuel Cells. Acs Nano. 2010;4(3):1321-6.

[47] Wen Z, Ci S, Zhang F, Feng X, Cui S, Mao S, et al. Nitrogen-Enriched Core-Shell Structured Fe/Fe3C-C Nanorods as Advanced Electrocatalysts for Oxygen Reduction Reaction. Adv Mater. 2012;24(11):1399-404.
[48] Hou Y, Huang T, Wen Z, Mao S, Cui S, Chen J. Metal−Organic Framework-Derived Nitrogen-Doped Core-Shell-Structured Porous Fe/Fe3C@C Nanoboxes Supported on Graphene Sheets for Efficient Oxygen Reduction Reactions. Adv Energy Mater. 2014;4(11):n/a-n/a.
[49] Yang W, Liu X, Yue X, Jia J, Guo S. Bamboo-like Carbon Nanotube/Fe3C Nanoparticle Hybrids and Their Highly Efficient Catalysis for Oxygen Reduction. J Am Chem Soc. 2015;137(4):1436-9.
[50] Liu B, Soares P, Checkles C, Zhao Y, Yu G. Three-Dimensional Hierarchical Ternary Nanostructures for High-Performance Li-Ion Battery Anodes. Nano Letters. 2013;13(7):3414-9.
[51] Wepasnick KA, Smith BA, Schrote KE, Wilson HK, Diegelmann SR, Fairbrother DH. Surface and structural characterization of multi-walled carbon nanotubes following different oxidative treatments. Carbon. 2011;49(1):24-36.
[52] Feng X, Irle S, Witek H, Morokuma K, Vidic R, Borguet E. Sensitivity of Ammonia Interaction with Single-Walled Carbon Nanotube Bundles to the Presence of Defect Sites and Functionalities. Journal of the American Chemical Society. 2005;127(30):10533-8.
[53] Koroteev VO, Bulusheva LG, Asanov IP, Shlyakhova EV, Vyalikh DV, Okotrub AV. Charge Transfer in the MoS2/Carbon Nanotube Composite. The Journal of Physical Chemistry C. 2011;115(43):21199-204.
[54] Kong D, Wang H, Cha JJ, Pasta M, Koski KJ, Yao J, et al. Synthesis of MoS2 and MoSe2 Films with Vertically Aligned Layers. Nano Letters. 2013;13(3):1341-7.
[55] Antunes EF, Lobo AO, Corat EJ, Trava-Airoldi VJ, Martin AA, Veríssimo C. Comparative study of first- and second-order Raman spectra of MWCNT at visible and infrared laser excitation. Carbon. 2006;44(11):2202-11.
[56] Gonçalves AG, Figueiredo JL, Órfão JJM, Pereira MFR. Influence of the surface chemistry of multi-walled carbon nanotubes on their activity as ozonation catalysts. Carbon. 2010;48(15):4369-81.
[57] Datsyuk V, Kalyva M, Papagelis K, Parthenios J, Tasis D, Siokou A, et al. Chemical oxidation of multiwalled carbon nanotubes. Carbon. 2008;46(6):833-40.
[58] Kim YJ, Shin TS, Choi HD, Kwon JH, Chung Y-C, Yoon HG. Electrical conductivity of chemically modified multiwalled carbon nanotube/epoxy composites. Carbon. 2005;43(1):23-30.
[59] Zhou G, Li F, Cheng H-M. Progress in flexible lithium batteries and future prospects. Energy & Environmental Science. 2014;7(4):1307-38.
[60] Shi Y, Wang Y, Wong JI, Tan AYS, Hsu C-L, Li L-J, et al. Self-assembly of hierarchical MoSx/CNT nanocomposites (2<x<3): towards high performance anode materials for lithium ion batteries. Scientific Reports. 2013;3.
[61] Song XC, Zheng YF, Zhao Y, Yin HY. Hydrothennal synthesis and characterization of CNT@MoS2 nanotabes. Materials Letters. 2006;60(19):2346-8.
[62] Yan Y, Ge X, Liu Z, Wang J-Y, Lee J-M, Wang X. Facile synthesis of low crystalline MoS2 nanosheet-coated CNTs for enhanced hydrogen evolution reaction. Nanoscale. 2013;5(17):7768-71.
[63] Kang K, Meng YS, Bréger J, Grey CP, Ceder G. Electrodes with High Power and High Capacity for Rechargeable Lithium Batteries. Science. 2006;311(5763):977-80.
[64] Du G, Guo Z, Wang S, Zeng R, Chen Z, Liu H. Superior stability and high capacity of restacked molybdenum disulfide as anode material for lithium ion batteries. Chemical Communications. 2010;46(7):1106-8.
[65] Chang K, Chen WX. L-Cysteine-Assisted Synthesis of Layered MoS2/Graphene Composites with Excellent Electrochemical Performances for Lithium Ion Batteries. Acs Nano. 2011;5(6):4720-8.
[66] Wang C, Wan W, Huang YH, Chen JT, Zhou HH, Zhang XX. Hierarchical MoS2 nanosheet/active carbon fiber cloth as a binder-free and free-standing anode for lithium-ion batteries. Nanoscale. 2014;6(10):5351-8.

[67] Chang K, Chen WX, Ma L, Li H, Li H, Huang FH, et al. Graphene-like MoS2/amorphous carbon composites with high capacity and excellent stability as anode materials for lithium ion batteries. J Mater Chem. 2011;21(17):6251-7.
[68] Rahman MA, Song GS, Bhatt AI, Wong YC, Wen CE. Nanostructured Silicon Anodes for High-Performance Lithium-Ion Batteries. Advanced Functional Materials. 2016;26(5):647-78.
[69] Piper DM, Evans T, Xu SS, Kim SC, Han SS, Liu KL, et al. Optimized Silicon Electrode Architecture, Interface, and Microgeometry for Next-Generation Lithium-Ion Batteries. Advanced Materials. 2016;28(1):188-+.
[70] Scrosati B, Hassoun J, Sun YK. Lithium-ion batteries. A look into the future. Energy & Environmental Science. 2011;4(9):3287-95.
[71] Hou Y, Li J, Wen Z, Cui S, Yuan C, Chen J. Co3O4 nanoparticles embedded in nitrogen-doped porous carbon dodecahedrons with enhanced electrochemical properties for lithium storage and water splitting. Nano Energy. 2015;12:1-8.
[72] Li J, Hou Y, Gao X, Guan D, Xie Y, Chen J, et al. A three-dimensionally interconnected carbon nanotube/layered MoS2 nanohybrid network for lithium ion battery anode with superior rate capacity and long-cycle-life. Nano Energy. 2015;16:10-8.
[73] McDowell MT, Lee SW, Nix WD, Cui Y. 25th Anniversary Article: Understanding the Lithiation of Silicon and Other Alloying Anodes for Lithium-Ion Batteries. Advanced Materials. 2013;25(36):4966-84.
[74] Hou Y, Li J, Wen Z, Cui S, Yuan C, Chen J. N-doped graphene/porous g-C3N4 nanosheets supported layered-MoS2 hybrid as robust anode materials for lithium-ion batteries. Nano Energy. 2014;8:157-64.
[75] Han H, Song T, Bae JY, Nazar LF, Kim H, Paik U. Nitridated TiO2 hollow nanofibers as an anode material for high power lithium ion batteries. Energy & Environmental Science. 2011;4(11):4532-6.
[76] Landi BJ, Ganter MJ, Cress CD, DiLeo RA, Raffaelle RP. Carbon nanotubes for lithium ion batteries. Energy & Environmental Science. 2009;2(6):638-54.
[77] Song T, Jeon Y, Samal M, Han H, Park H, Ha J, et al. A Ge inverse opal with porous walls as an anode for lithium ion batteries. Energy & Environmental Science. 2012;5(10):9028-33.
[78] Wen ZH, Lu GH, Mao S, Kim H, Cui SM, Yu KH, et al. Silicon nanotube anode for lithium-ion batteries. Electrochemistry Communications. 2013;29:67-70.
[79] Chan CK, Patel RN, O'Connell MJ, Korgel BA, Cui Y. Solution-Grown Silicon Nanowires for Lithium-Ion Battery Anodes. Acs Nano. 2010;4(3):1443-50.
[80] Liu NA, Hu LB, McDowell MT, Jackson A, Cui Y. Prelithiated Silicon Nanowires as an Anode for Lithium Ion Batteries. Acs Nano. 2011;5(8):6487-93.
[81] Luo LL, Yang H, Yan PF, Travis JJ, Lee Y, Liu N, et al. Surface-Coating Regulated Lithiation Kinetics and Degradation in Silicon Nanowires for Lithium Ion Battery. Acs Nano. 2015;9(5):5559-66.
[82] Huang XK, Kim H, Cui SM, Hurley PT, Chen JH. Si-Composite Anode for Lithium-Ion Batteries with High Initial Coulombic Efficiency. Energy Technology. 2013;1(5-6):305-8.
[83] Huang XK, Pu HH, Chang JB, Cui SM, Hallac PB, Jiang JW, et al. Improved Cyclic Performance of Si Anodes for Lithium-Ion Batteries by Forming Intermetallic Interphases between Si Nanoparticles and Metal Microparticles. Acs Applied Materials & Interfaces. 2013;5(22):11965-70.
[84] Liu X, Zhao HL, Xie JY, Lv PP, Wang K, Cui JJ. SiOx (0 < x <= 2) Based Anode Materials for Lithium-Ion Batteries. Progress in Chemistry. 2015;27(4):336-48.
[85] Chang JB, Huang XK, Zhou GH, Cui SM, Hallac PB, Jiang JW, et al. Multilayered Si Nanoparticle/Reduced Graphene Oxide Hybrid as a High-Performance Lithium-Ion Battery Anode. Advanced Materials. 2014;26(5):758-64.
[86] Cui LF, Yang Y, Hsu CM, Cui Y. Carbon-Silicon Core-Shell Nanowires as High Capacity Electrode for Lithium Ion Batteries. Nano Letters. 2009;9(9):3370-4.
[87] Luo LL, Zhao P, Yang H, Liu BR, Zhang JG, Cui Y, et al. Surface Coating Constraint Induced Self-Discharging of Silicon Nanoparticles as Anodes for Lithium Ion Batteries. Nano Letters. 2015;15(10):7016-22.

[88] Lotfabad EM, Kalisvaart P, Cui K, Kohandehghan A, Kupsta M, Olsen B, et al. ALD TiO2 coated silicon nanowires for lithium ion battery anodes with enhanced cycling stability and coulombic efficiency. Physical Chemistry Chemical Physics. 2013;15(32):13646-57.
[89] Quiroga-Gonzalez E, Carstensen J, Glynn C, O'Dwyer C, Foll H. Pore size modulation in electrochemically etched macroporous p-type silicon monitored by FFT impedance spectroscopy and Raman scattering. Physical Chemistry Chemical Physics. 2014;16(1):255-63.
[90] Yu DP, Bai ZG, Ding Y, Hang QL, Zhang HZ, Wang JJ, et al. Nanoscale silicon wires synthesized using simple physical evaporation. Applied Physics Letters. 1998;72(26):3458-60.
[91] Chang J, Huang X, Zhou G, Cui S, Hallac PB, Jiang J, et al. Multilayered Si Nanoparticle/Reduced Graphene Oxide Hybrid as a High-Performance Lithium-Ion Battery Anode. Advanced Materials. 2014;26(5):758-64.
[92] Yao Y, Liu N, McDowell MT, Pasta M, Cui Y. Improving the cycling stability of silicon nanowire anodes with conducting polymer coatings. Energy & Environmental Science. 2012;5(7):7927-30.
[93] Zhou X, Yin Y-X, Wan L-J, Guo Y-G. Facile synthesis of silicon nanoparticles inserted into graphene sheets as improved anode materials for lithium-ion batteries. Chemical Communications. 2012;48(16):2198-200.
[94] Hummers WS, Offeman RE. Preparation of Graphitic Oxide. J Am Chem Soc. 1958;80(6):1339-.
[95] Shen A, Zou Y, Wang Q, Dryfe RAW, Huang X, Dou S, et al. Oxygen Reduction Reaction in a Droplet on Graphite: Direct Evidence that the Edge Is More Active than the Basal Plane. Angewandte Chemie International Edition. 2014;53(40):10804-8.
[96] Pimenta MA, Dresselhaus G, Dresselhaus MS, Cancado LG, Jorio A, Saito R. Studying disorder in graphite-based systems by Raman spectroscopy. Phys Chem Chem Phys. 2007;9(11):1276-90.
[97] Mao S, Wen Z, Huang T, Hou Y, Chen J. High-performance bi-functional electrocatalysts of 3D crumpled graphene-cobalt oxide nanohybrids for oxygen reduction and evolution reactions. Energ Environ Sci. 2014;7(2):609-16.
[98] Liang Y, Li Y, Wang H, Zhou J, Wang J, Regier T, et al. Co3O4 nanocrystals on graphene as a synergistic catalyst for oxygen reduction reaction. Nat Mater. 2011;10(10):780-6.
[99] Mayrhofer KJJ, Strmcnik D, Blizanac BB, Stamenkovic V, Arenz M, Markovic NM. Measurement of oxygen reduction activities via the rotating disc electrode method: From Pt model surfaces to carbon-supported high surface area catalysts. Electrochim Acta. 2008;53(7):3181-8.
[100] Chang K, Chen W, Ma L, Li H, Li H, Huang F, et al. Graphene-like MoS2/amorphous carbon composites with high capacity and excellent stability as anode materials for lithium ion batteries. Journal of Materials Chemistry. 2011;21(17):6251-7.
[101] Fu K, Yildiz O, Bhanushali H, Wang Y, Stano K, Xue L, et al. Aligned Carbon Nanotube-Silicon Sheets: A Novel Nano-architecture for Flexible Lithium Ion Battery Electrodes. Advanced Materials. 2013;25(36):5109-14.
[102] Kim G, Jeong S, Shin J-H, Cho J, Lee H. 3D Amorphous Silicon on Nanopillar Copper Electrodes as Anodes for High-Rate Lithium-Ion Batteries. Acs Nano. 2014;8(2):1907-12.
[103] Zhu Z, Wang S, Du J, Jin Q, Zhang T, Cheng F, et al. Ultrasmall Sn Nanoparticles Embedded in Nitrogen-Doped Porous Carbon As High-Performance Anode for Lithium-Ion Batteries. Nano Letters. 2014;14(1):153-7.
[104] Nguyen HT, Yao F, Zamfir MR, Biswas C, So KP, Lee YH, et al. Highly Interconnected Si Nanowires for Improved Stability Li-Ion Battery Anodes. Advanced Energy Materials. 2011;1(6):1154-61.
[105] Zhou X, Yin Y-X, Wan L-J, Guo Y-G. Self-Assembled Nanocomposite of Silicon Nanoparticles Encapsulated in Graphene through Electrostatic Attraction for Lithium-Ion Batteries. Adv Energy Mater. 2012;2(9):1086-90.
[106] Qin J, He C, Zhao N, Wang Z, Shi C, Liu E-Z, et al. Graphene Networks Anchored with Sn@Graphene as Lithium Ion Battery Anode. Acs Nano. 2014;8(2):1728-38.

[107] Hwang J, Woo SH, Shim J, Jo C, Lee KT, Lee J. One-Pot Synthesis of Tin-Embedded Carbon/Silica Nanocomposites for Anode Materials in Lithium-Ion Batteries. Acs Nano. 2013;7(2):1036-44.
[108] Xu Y, Liu Q, Zhu Y, Liu Y, Langrock A, Zachariah MR, et al. Uniform Nano-Sn/C Composite Anodes for Lithium Ion Batteries. Nano Letters. 2013;13(2):470-4.